DESIGN, FABRICATION AND MEASUREMENT OF HYBRID FREQUENCY SELECTIVE SURFACE (FSS) RADOMES

A THESIS

SUBMITTED TO THE DEPARTMENT OF ELECTRICAL AND

ELECTRONICS ENGINEERING

AND THE INSTITUTE OF ENGINEERING AND SCIENCE

OF BİLKENT UNIVERSITY

IN PARTIAL FULFILLMENT OF THE REQUIREMENTS

FOR THE DEGREE OF

MASTER OF SCIENCE

By

Özkan Sağlam

July 2009

I certify that I have read this thesis and that in my opinion it is fully adequate, in scope and in quality, as a thesis for the degree of Master of Science.

Assoc. Prof. Vakur B. Ertürk(Supervisor)

I certify that I have read this thesis and that in my opinion it is fully adequate, in scope and in quality, as a thesis for the degree of Master of Science.

Prof. Dr. Ayhan Altıntaş

I certify that I have read this thesis and that in my opinion it is fully adequate, in scope and in quality, as a thesis for the degree of Master of Science.

Prof. Dr. Gülbin Dural

Approved for the Institute of Engineering and Science:

Prof. Dr. Mehmet Baray
Director of Institute of Engineering and Science

ABSTRACT

DESIGN, FABRICATION AND MEASUREMENT OF HYBRID FREQUENCY SELECTIVE SURFACE (FSS) RADOMES

Özkan Sağlam
M.S. in Electrical and Electronics Engineering
Supervisor: Assoc. Prof. Vakur B. Ertürk
July 2009

In modern military platforms such as ships, aircrafts and missiles, frequency selective surfaces (FSS) are widely used for antennas and radar cross section (RCS) reduction. The RCS of complicated objects such as antennas are difficult or impossible to control over a wide frequency range. The most efficient and cost-effective approach in these situations is to shield the scattering object from the threat radars by making use of wide-band radar absorbing material (RAM) coating. If the object is an antenna, then obviously, the system served by this antenna cannot operate when it is stowed. An alternate approach is to cover the antenna with an FSS that is transparent at the antenna operating frequency, yet opaque at the threat radar frequencies.

In this thesis, different types of FSS structures comprising slot elements and modified loop elements, namely single polarized loop FSS, have been investigated intensively with their applications to hybrid FSS radomes. Their resonance mechanisms and transmission properties are examined in detail. The main focus of the thesis is to design a hybrid FSS radome based on different unit element types. Complex dielectric constant measurements are conducted as an

input to the FSS radome design. Experimental results based on measuring the transmission curves of fabricated radome prototypes are supported by computer simulations. Transmission properties of the slot FSS structures and the single polarized loop FSS structures have been compared and discussed. In contrast with most of the published work in literature, transmission measurements are supported by the radiation performance measurements. Adaptation of the single polarized loop FSS radome to the slotted waveguide antenna has been achieved without any significant reduction in the radiation performance. The antenna with this metallic radome has the advantage of superior mechanical durability as well as reduced out-of-band RCS.

Keywords: Frequency Selective Surface (FSS), space filter, hybrid radome, RCS reduction, dielectric measurement

ÖZET

HİBRİT FREKANS SEÇİCİ YÜZEY (FSY) RADOM TASARIM, ÜRETİM VE ÖLÇÜMÜ

Özkan Sağlam
Elektrik ve Elektronik Mühendisliği Bölümü Yüksek Lisans
Tez Yöneticisi: Doç. Dr. Vakur B. Ertürk
Temmuz 2009

Frekans seçici yüzeyler (FSY), gemi, uçak ve füze gibi modern askeri platformlarda antenler ve radar kesit alan (RKA) azaltımı için yaygın olarak kullanılmaktadır. Antenler gibi karmaşık nesnelerin radar kesit alanlarını geniş bir frekans bandı boyunca kontrol altında tutabilmek epeyce zor veya imkansızdır. Bu gibi durumlarda en verimli ve maliyeti düşük yöntem, saçılım yaratan nesneyi geniş bantlı radar soğurucu malzeme (RSM) kaplama ile tehdit radarlara karşı siperlemektir. Eğer söz konusu nesne anten ise; apaçıktır ki, bu anten saklandığı zaman işlevini yerine getiremez. Başka bir yaklaşım tarzı ise anteni, çalışma frekansında saydam, tehdit radar frekanslarında opak FSY ile kaplamaktır.

Bu tezde, yarık elemanlar ve değiştirilmiş halka elemanlardan (tek kutuplu halka FSY) oluşan değişik tipte FSY yapıları hibrit radom uygulamaları ile birlikte derinlemesine incelenmiştir. Rezonans frekansları ve iletim özellikleri detaylı olarak irdelenmiştir. Tezin esas odak noktası değişik birim eleman tiplerine dayalı hibrit FSY radomlar tasarlamaktır. FSY radom tasarımına girdi sağlaması bakımından karmaşık dielektrik sabiti ölçümleri yürütülmüştür. Üretilen radom prototipleriyle yapılan ölçüm sonuçları bilgisayar benzetimleriyle

desteklenmiştir. Yarık ve tek kutuplu halka FSYlerin iletim özellikleri karşılaştırılıp tartışılmıştır. Literatürdeki çoğu çalışmadan farklı olarak, geçirgenlik ölçümleri ışıma performansı ölçümleri ile desteklenmiştir. Tek kutuplu halka FSY radomun yarıklı dalga kılavuzu antene uyarlanması anten ışıma performansında kayda değer bir azalma olmaksızın başarılmıştır. Metal radom sayesinde anten, üstün mekanik mukavemet ve bant dışı RKA azaltımı avantajlarına sahiptir.

Anahtar Kelimeler: Frekans Seçici Yüzey (FSY), uzay filtre, hibrit radom, RKA azaltımı, dielektrik ölçümü

ACKNOWLEDGMENTS

I would like express my gratitude and my endless thanks to my supervisor Assoc. Prof. Vakur B. Ertürk for his supervision and invaluable guidance during the development of this thesis.

I would like to thank Prof. Ayhan Altıntaş and Prof. Gülbin Dural, the members of my jury, for accepting to read and review the thesis.

I would like to express my gratitude to my company Aselsan Inc. for letting me involve in this thesis and also to use their fabrication and measurement facilities. I am grateful to Mehmet Erim İnal and Can Barış Top for their valuable comments and support throughout the development of this thesis.

I would also like to thank Turkish Scientific and Technological Research Council for their financial assistance during my graduate study.

Contents

List of Figures

List of Tables

$$\nabla \times \mathbf{E} = -j\omega\mu\mathbf{H}$$

$$\nabla \times \mathbf{H} = j\omega\epsilon\mathbf{E} + \mathbf{J_i}$$

$$\nabla \cdot \mathbf{D} = \rho$$

$$\nabla \cdot \mathbf{B} = 0$$

Chapter 1

Introduction

Frequency Selective Surfaces (FSSs) have been the subject of intensive investigation for their widespread applications as spatial microwave and optical filters for more than four decades [1]-[6]. Frequency selective surfaces are usually constructed from periodically arranged metallic patches of arbitrary geometries or their complimentary geometry having aperture elements similar to patches within a metallic screen. These surfaces exhibit total reflection or transmission, for the patches and apertures, respectively, in the neighborhood of the element resonances. The most important step in the design process of a desired FSS is the proper choice of constituting elements for the array. The element type and geometry, the substrate parameters, the presence or absence of superstrates, and inter-element spacing generally determine the overall frequency response of the structure, such as its bandwidth, transfer function, and its dependence on the incidence angle and polarization. Although conceptually similar to a classical microwave filter, it should be emphasized that a *space filter* is inherently much more complicated. First of all, a classical filter merely has a pair of input and output terminals and only the frequency is varied at the input while the response at the output is recorded. A space filter, on the other hand, has the incident field arriving at various angles of incidence as well as polarizations. This fact has a

profound effect on the transmission properties; in short, the transmission curve will change dramatically unless carefully designed. The shapes and configurations that can be chosen for the FSS elements are limited only by the imagination of the designer.

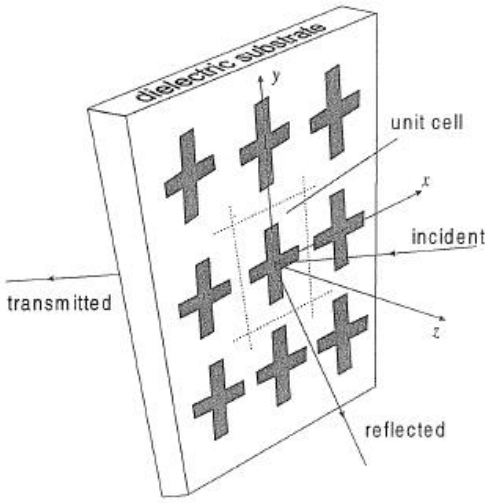

Figure 1.1: Perspective of a Crossed-dipole Periodic Array

The unique properties and practical uses of frequency selective surfaces realized over many years have produced an extensive body of work within both academic and industrial sectors. Historically, the essential behavior of these surfaces stems from meshes and strip gratings concepts exploited in the optical regime. At microwave frequencies, the applications of FSSs are predominantly for antenna systems in fixed as well as mobile services. Published reports of basic properties of simple structures in the cm-wave region go back as far as 1946 [7]-[8], although the name FSS was not used until much later on. Planar and curved FSSs are used for a variety of applications including design of antenna radomes, dichroic surfaces for reflectors and subreflectors of large aperture antennas, or even absorbers [9]. More sophisticated FSSs with multiple resonances [10] have been designed and reported in the literature with the advent of computational electromagnetics codes that began in the 1980's [11]. More recently, advanced methods based on method of moments (MoM), finite element method (FEM),

and finite-difference time-domain (FDTD) with periodic boundary conditions have made the design process of FSSs substantially easier. In [12], self-similarity characteristics of fractal geometries are exploited for the design of a dual-band FSS. In [13], design of a reconfigurable frequency selective surface with traditional elements integrated with RF MEMS switches operating at Ka-band is reported. Also the application of ferroelectric substrates for tuning the surface frequency behavior is considered in [14]. The use of superconductors in the design of very low loss FSSs is comprehensively studied in [15].

In modern military platforms such as ships, aircrafts and missiles, frequency selective surfaces are widely used for antennas and radar cross section (RCS) reduction. The RCSs of complicated objects such as antennas are difficult or impossible to control over a wide frequency range [16]. The most efficient and cost-effective approach in these situations is to shield the scattering object from the threat radar. This can be accomplished by retracting the object and covering the cavity in which it is housed with a shutter. If the object is an antenna, then, obviously, the system served by this antenna cannot operate when it is stowed. An alternate approach is to cover the antenna with an FSS that is transparent at the antenna operating frequency, yet opaque at the threat radar frequency. Considering the shape and structural constraints of military platforms, the antenna and the FSS radome should be carefully designed as an integrated module such that the module should have the radiation performance of the antenna, and the filtering performance for anti-interference and low RCS. Otherwise, a bad design such as setting up the antenna behind an FSS radome blindly may lead to an increase in the RCS, a degradation of the radiation performance of the antenna as well as its impedance matching properties, strong undesired electromagnetic interference (that may destroy the whole electronics of the system), etc.

In literature very few papers can be found about an integrated design of antenna and FSS radome. Structural integration of antenna and an FSS structure was firstly reported in [17]. But in [17] FSS was used only to enhance the antenna radiation efficiency due to its high impedance characteristic. Multilayer FSS combined with open-end waveguide radiator arrays have been presented in [18]-[20], in which only filtering performance of the integrated module has been investigated using multi mode equivalent network method.

The aim of this thesis is to propose a metallic hybrid radome formed as a composite multi-layered structure utilizing frequency selective conductive sheets. The idea is based on employing slot type resonant elements periodically on a conducting sheet. This structure is expected to behave like a band-pass filter. Because, the overall structure is transparent to electromagnetic waves at the resonant frequency of the slot elements with a certain bandwidth and is opaue to electromagnetic waves outside this bandwidth. Moreover, the band-pass filter characteristics required in this thesis are to have an almost flat top at the pass band and to have a fast roll-off. Thus, two periodic surfaces are cascaded behind each other by optimizing the coupling between the layers. Besides, the use of outer dielectric strata provides constant bandwidth characteristic over a wide range of angle of incidence. The intermediate dielectric layer has an effective dielectric function selected to achieve a critical array coupling between the FSS layers. Dielectric properties of both the outer and the intermediate layers are measured initially for their accurate modeling throughout the FSS radome design.

In this thesis, frequency selective surfaces based on different unit elements are designed, simulated, fabricated and tested. Frequency responses of the FSSs and possible effects on the radiation performance of the antenna, to be covered with FSS radome, are examined in a comparative manner. In contrast to most of the published works in the open literature, in addition to free-space transmission

measurements of the fabricated FSS, we present the measured radiation patterns of a slotted waveguide array (SWGA) covered with the designed FSS radome.

In Chapter 2, a detailed investigation of periodic surfaces including their resonance mechanisms, analysis method and some unit element types are provided. Chapter 3 presents some material measurement methods one of which we use for the characterization of dielectric materials to be used in FSS structures. The free-space dielectric measurement setup is explained in detail along with the implemented advanced calibration techniques. In Chapter 4, numerical and experimental filter characteristics of different FSS prototypes are provided with a comparative analysis of their frequency responses. The radiation pattern measurements of a slotted waveguide antenna with/without FSS radome prototypes carried out in the near-field test range are presented in Chapter 5. Effects of FSS radome to the antenna radiation performance are investigated for all radome prototypes comparatively. An e^{jwt} time convension is used, where $w = 2\pi f$ with f being the operating frequency.

Chapter 2

Overview of Periodic Surfaces

2.1 Introduction

A *periodic surface* is basically an assembly of identical elements arranged in a one- or two-dimensional array [9]. Fundamentally, any periodic array can be excited in two ways: by an incident plane wave (passive array), or by individual generators connected to each element (active array). FSSs are essentially passive array structures which consist of thin conducting elements, often printed on a dielectric substrate for support. They behave as passive electromagnetic filters for incoming plane waves. Frequently, these arrays take the form of periodic apertures in a conducting plane, Babinet's complement of the former. Figure 2.1 shows a typical reflection coefficient response of an array of dipoles/slots, whereby polarized incident waves are reflected/transmitted by the surface at some frequencies, whilst the surface is transparent/opaque to these waves at other frequencies.

For the conducting (dipole) array case the resonance is due to high element currents induced, which are small near the pass-band. The surface is acting like a metallic sheet at resonance. If an array of apertures (slots) is to be used, this perforated screen is mostly reflective and exhibits a pass-band at resonance

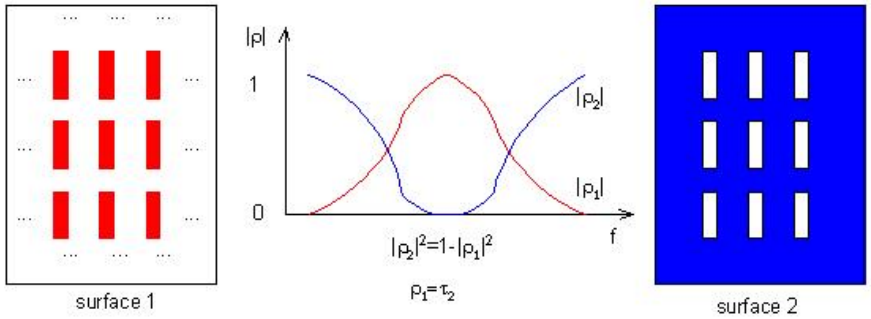

Figure 2.1: Typical frequency response for array of dipoles (red) vs. slots (blue)

which results from strong fields in the apertures. Throughout this work, we will mostly give emphasis to the aperture array case since FSS will be implemented as a band-pass radome enclosing the antenna.

In this thesis, unit-cell simulation, which is available in CST Microwave Studio® 2008 commercial software [36], is employed for the analysis of periodic FSS structures.

2.2 The Unit Cell Approach

In this section, a brief explanation of method of analysis for FSSs is presented. As mentioned before, FSSs are *periodic* arrangements of metallic patches of arbitrary geometries or their complimentary geometries having aperture elements similar to patches within a metallic screen. Taking the two dimensional periodicity into account, the analysis of FSS structures is simplified by use of the Floquet's theorem.

Consider the two dimensional $infinite \times infinite$ periodic dipole array shown in Figure 2.2. We will denote each infinite column by a number q, and each infinite row by a number m. The inter-element spacings in the x-direction (D_x) are the same for all rows, and inter-element spacings in the z-direction (D_z) are

the same for all columns. The array is planar in both x- and z-directions with all elements identical to each other.

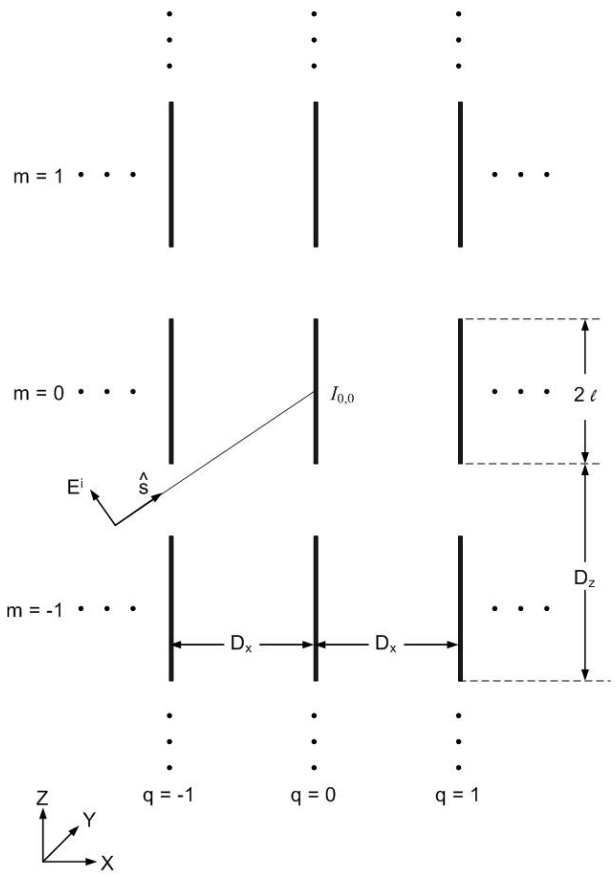

Figure 2.2: An $infinite \times infinite$ periodic structure with inter-element spacings D_x and D_z and element length $2l$

If this structure is exposed to an incident plane wave propagating in the direction

$$\hat{s} = \hat{x}s_x + \hat{y}s_y + \hat{z}s_z, \tag{2.1}$$

it will induce the current I_{qm} in the element of column q and row m. The amplitude of all the element currents will be the same, while their phases will match the phase of the incident field. The element current in column q and row m will be,

$$I_{qm} = I_{0,0}e^{-j\beta_q D_x s_x}e^{-j\beta_m D_z s_z} \tag{2.2}$$

as a direct consequence of Floquet's theorem [21] which is outlined in Appendix A.

In this thesis, unit-cell simulation, which is available in CST Microwave Studio® 2008 commercial software [36], is employed for the analysis of periodic FSS structures. CST Microwave Studio® is a 3D full wave solver utilizing finite integration method. Periodic boundary condition (PBC) together with Floquet's theorem enables us to analyze only one constituting element of the array as if there were infinite periodic elements. This reference element is named as *unit-cell*, therefore, periodic boundary condition together with phase shifts between the neighboring cells is sometimes called as *unit-cell boundary*. In the unit-cell simulation, we illuminate the FSS with a plane wave from the front and compute the transmission coefficient through the FSS (also reflection coefficient off the FSS), applying the unit-cell boundary condition to the four sides of FSS and radiation boundaries to the front and back of the unit-cell.

Figure 2.3 shows the simulation view of two FSS layers printed on a dielectric slab and separated by air gaps in between. The unit-cell boundaries are applied in x- and y-directions implying that the structure is of infinite extent in these directions. The incident plane wave propagates in the z-direction. As well as normal incident plane waves, oblique incident plane waves can also be impinged on the structure.

Since we analyze only the unit-cell rather than the array itself, this method offers a quick way to compute the frequency response of FSS configurations of interest. For this reason, we adopt the unit-cell approach to simulate the characteristics of FSSs in this thesis.

2.3 Shaping The Resonant Curve

Ordinary periodic surfaces exhibit perfect reflection or transmission only at the resonance frequency determined by geometrical properties of unit elements. Filter selectivity of these surfaces are in general inadequate and spectral shaping

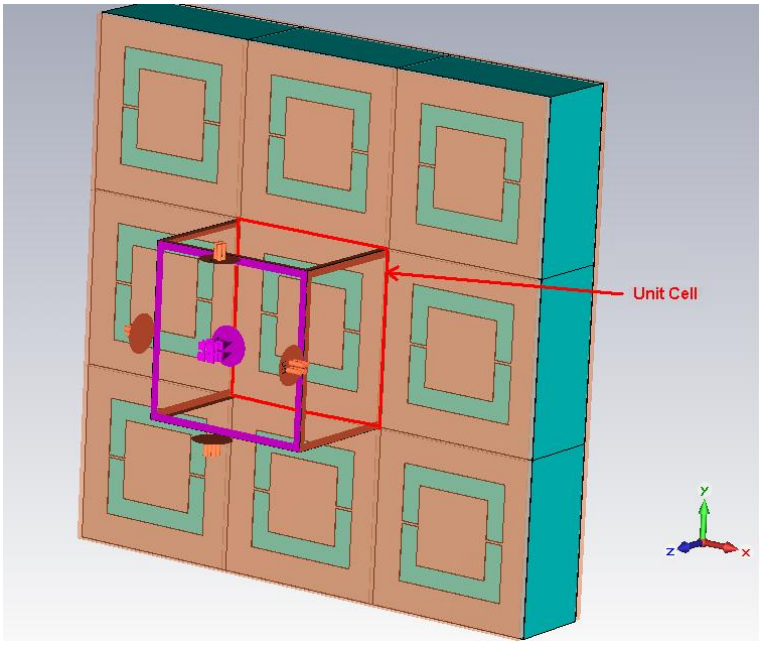

Figure 2.3: Illustration of unit-cell boundaries

they offer is poor. However, many applications such as radomes call for a resonant curve with a flat top and sharper roll-off. Munk, who has been the guru of FSS technology since early 1970s, advises two ways to accomplish this goal [9]:

- Cascading two or more periodic surfaces behind each other without dielectrics.
- Using dielectric slabs between cascading periodic surfaces, which leads to the so-called *hybrid periodic surfaces*.

2.3.1 Single vs. Multilayer Periodic Surfaces

The reflection of a plane wave from an array of loaded or unloaded dipoles was determined in [5] using a mutual impedance approach. Munk *et al.* [6] further extended this method to include two parallel displaced arrays of loaded dipoles. An improved band-stop filter characteristics can be obtained by mounting two arrays behind each other.

As a consequence of Babinet's principle and duality, it is well known from electromagnetic theory that the complement of a planar metallic structure can be obtained by replacing the metal parts of the original structure with apertures, and apertures with metal plates. If the metal plate is infinitesimally thin and perfectly conducting then the apertures behave as perfect magnetic conductors. Since the dipoles in [5]-[6] are infinitesimally thin and perfectly conducting, we can by duality theorem replace these dipoles with complementary slots and obtain transmission curves similar to the reflection curves of [5]. Furthermore, cascading these slot arrays properly as outlined in [6], we shall attain enhanced band-pass filter characteristics.

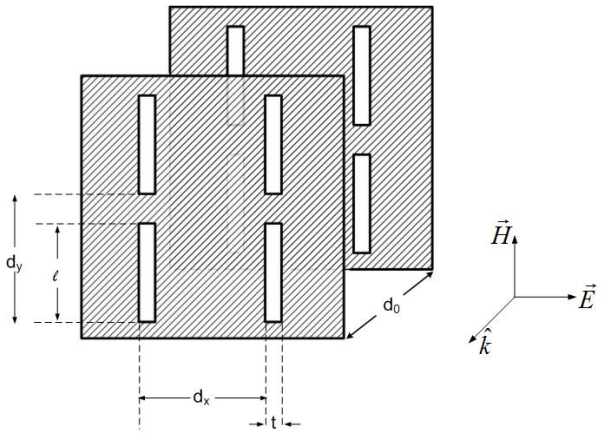

Figure 2.4: Cascaded slot arrays with dimensions $d_x = d_y = 15mm$, $l = 12mm$, $t = 1.2mm$, $d_0 = 7mm$

Figure 2.4 shows an example of two periodic slot arrays cascaded behind each other separated by a distance d_0. Note that the electric field is polarized perpendicular to the slots and the magnetic field is in the direction of the slots as a result of duality.

Investigation of transmission curves in Figure 2.5 evidently shows that the double layer slot array has a much flatter top and faster roll-off as compared to the single layer. It is critical to pay utmost attention to the coupling between the layers so as to obtain the best spectral shaping required for a particular

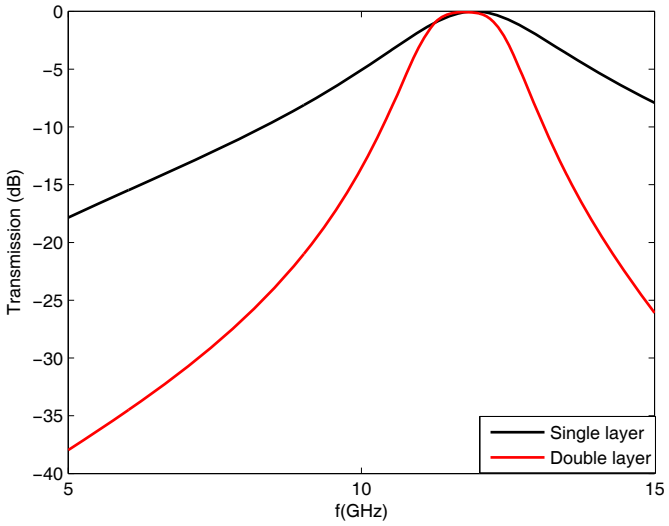

Figure 2.5: Transmission response for single vs. double layer slot arrays

application. In addition to this, the arrays must be well arranged in line because displaced arrays in E- or H-plane can yield transmission loss at resonance [6].

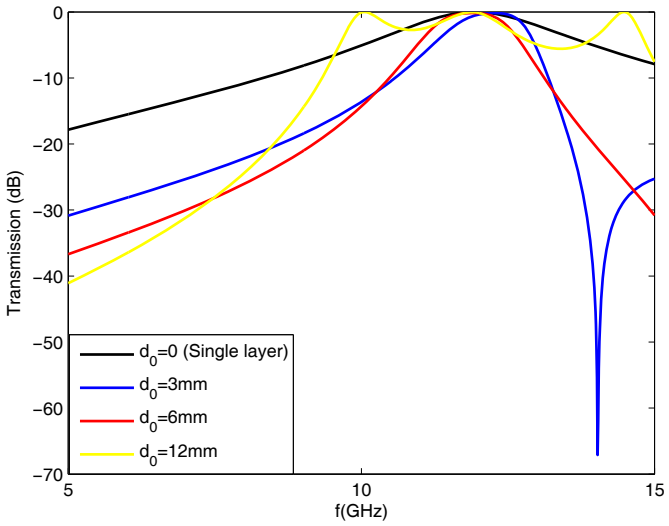

Figure 2.6: Transmission response for different separations

The transmission coefficient for double layer slot arrays has been analyzed for different array separations in order to find out the best filter curve. The single layer slot array has a resonance frequency of $f_0 \approx 12GHz$, which corresponds to a wavelength of $\lambda \approx 25mm$. Results presented in Figure 2.6 reveal that a

flat top and sharp roll-off in the frequency response can be obtained for $d_0 = 6mm$. As a result, the best filter curve for identical arrays is obtained when the electrical separation between the two arrays equals $\lambda/4$ (i.e., Butterworth). Since the electrical spacing between the arrays changes as the cosine of the angle of incidence, the present configuration is unable to provide an optimum filter curve for a wide range of incidence angles.

2.3.2 Dielectric Loading of Periodic Surfaces

Observations in the last section demonstrate that a resonant curve with a flat top and faster roll-off can be attained by cascading two slot arrays with an electrical spacing of $\lambda/4$ (or slightly less). However, this double layer slot array configuration without dielectric loading is inadequate in maintaining a constant bandwidth and resonant frequency for different angles of incidence.

Since the end of 1970s, the applications of rectangular slot elements were severely limited because of the change in resonant frequency and bandwidth with incidence angle. In 1978, Luebbers *et al.* [22] utilized a modal analysis solution which included the effects of dielectric slabs on both sides of the array and demonstrated that the dielectric effects can, with proper design, reduce or eliminate the unwanted changes in resonant frequency and bandwidth.

Figure 2.7 shows a single periodic surface provided with dielectric slabs of equal thickness and dielectric constant on each side. With such a surface we can obtain a bandwidth that is considerably larger than that of a single structure. In practice, dielectric slabs are used as supporting structures mainly for mechanical reasons since there is no *free-standing* array in real life.

The presence of dielectric medium around a periodic surface can profoundly change its resonant frequency. If the periodic structure had been completely surrounded by an infinite dielectric material of infinite extent and with relative

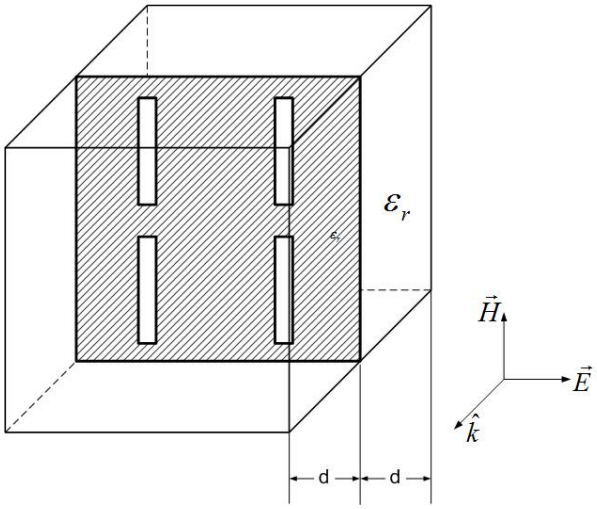

Figure 2.7: A single slotted surface with dielectric slabs on both sides

dielectric constant ϵ_r, it is easy to see from Maxwell's equations that the resonant frequency will reduce in frequency with the factor $\sqrt{\epsilon_r}$, as shown in Figure 2.8. If the extent of the infinite dielectric is reduced into dielectric slabs of a small, finite thickness $2d$, the resonant frequency will change to somewhere between f_0 and $f_0/\sqrt{\epsilon_r}$. It is interestingly observed from Figure 2.8 that even for slab thicknesses as small as $d \sim 0.05\lambda_\epsilon$, the resonant frequency is fairly close to $f_0/\sqrt{\epsilon_r}$.

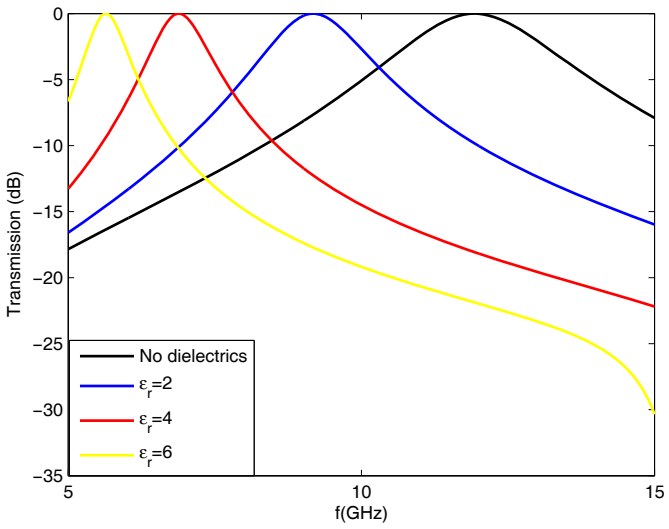

Figure 2.8: Effect of dielectric on the resonant frequency. Single layer slot array with $d = 1mm$ dielectric slabs of various ϵ_r on both sides

Although the resonant frequency shifts downwards with dielectric loading, this can be compensated by properly tuning the unit element parameters so that total transmission is shifted upwards to the original resonant frequency.

The main role of dielectric slabs on both side of the periodic surface is to maintain constant bandwidth and resonant frequency with changing angles of incidence as mentioned above. In order to investigate the effect of dielectric loading on the stabilization of bandwidth and resonant frequency, the periodic slot array in Figure 2.7 (with/without dielectric slabs) is illuminated with a plane wave of different incident angles. Figure 2.9 shows the transmission curves for different angles of incidence in the E-plane for the free-standing slot array with inter-element spacings $d_x = d_y = 15mm$, slot length $l = 12mm$ and slot thickness $t = 1.2mm$.

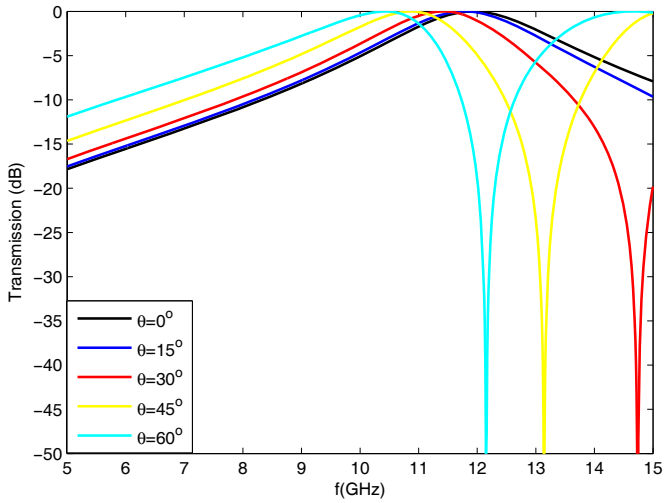

Figure 2.9: Transmission curves for the array of slots for different angles of incidence in E-plane

When the same slot array is loaded on both sides with dielectric slabs of thickness $d = 1mm$ and relative dielectric constant $\epsilon_r = 4$, the following transmission curves are obtained.

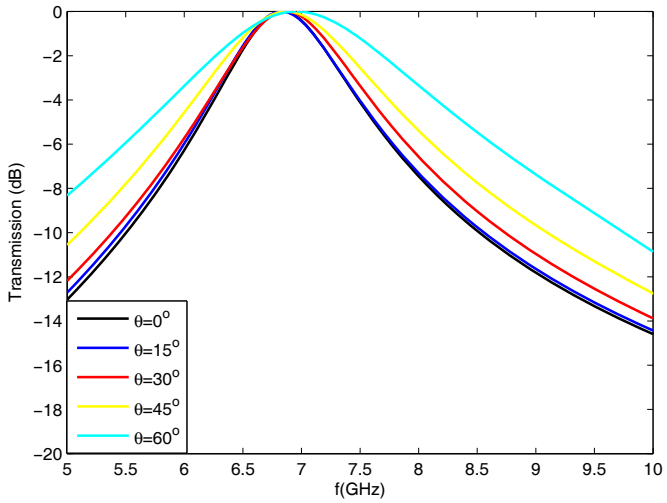

Figure 2.10: Transmission curves for the dielectric loaded slot array for different angles of incidence in E-plane

The resonant frequency of free-standing slot array shifts downwards as the angle of incidence increases whereas it is constant for wide range of incident angles when the array is loaded with dielectrics.

Angle of Incidence (deg)	Resonant Frequency (GHz)			
	Free-Standing Array		Dielectric Loaded Array	
	E-plane	H-plane	E-plane	H-plane
0	11.94	11.94	6.84	6.84
15	11.79	11.98	6.83	6.80
30	11.43	11.94	6.87	6.79
45	10.88	11.66	6.87	6.80
60	10.44	11.16	6.96	6.82

Table 2.1: Resonant frequencies of free-standing array vs. dielectric loaded array with slab thickness $d = 1mm$ and relative permittivity $\epsilon_r = 4$ on both sides

The last two columns of Table 2.1 clearly shows the stabilization of resonant frequency of dielectric loaded slot array for both E-plane and H-plane scans.

2.3.3 Real Hybrid Periodic Structures

In Section 2.3.1, the periodic surfaces have been cascaded without any dielectrics to obtain a transmission curve with a flat top and sharper roll-off. It has been concluded that multilayer slot array of Figure 2.4 has a transmission curve with a flat top and fast roll-off compared to that of a single layer slot array. However, frequency characteristics of multilayer slot arrays change dramatically as the angle of incident wave changes. Furthermore; in Section 2.3.2, it has been shown that resonant frequency as well as bandwidth of a periodic surface can be kept constant for different incident angles by use of dielectric slabs.

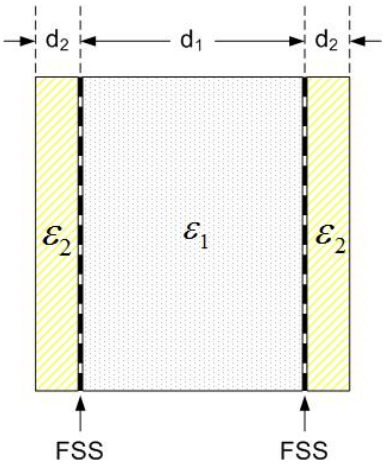

Figure 2.11: Cross section of the hybrid FSS radome

In this thesis, we will demonstrate a specific design that is comprised of two frequency selective surfaces sandwiched between three dielectric slabs as shown in Figure 2.11. With this profile, we can realize hybrid FSS radomes with high filter selectivity (i.e., fast roll-off and flat top) as well as constant resonant frequency and bandwidth with angle of incidence. The dielectric profile plays an important role in the design of hybrid radomes in maintaining constant bandwidth and flat top in the frequency response. Each dielectric slab in Figure 2.11 serves a specific purpose: The two outer ones preferably should be identical and are responsible for providing a constant bandwidth and resonant frequency for varying angle of incidence. Similarly the slab in the middle determines the flatness of the passband

of the transmission curve. It must be selected such that critical array coupling is achieved. Finally, the FSS determines the bandwidth and the resonant frequency of the overall structure.

2.4 Comparative Investigation of Element Types

The choice of the unit element plays a crucial role when designing a band-pass or band-stop FSS. Some elements are inherently more broad banded or more narrow-banded than others, while some can be varied considerably by design. Also the inter-element spacings as well as the element type can significantly change the bandwidth of an FSS: A larger spacing will in general produce a narrower bandwidth and vice versa.

The most common unit element types can be classified in groups as shown in Figure 2.12 [9].

In this section we will present a comparative investigation of the most common element types with their theory of operation, resonance mechanism and characterization via parametric study.

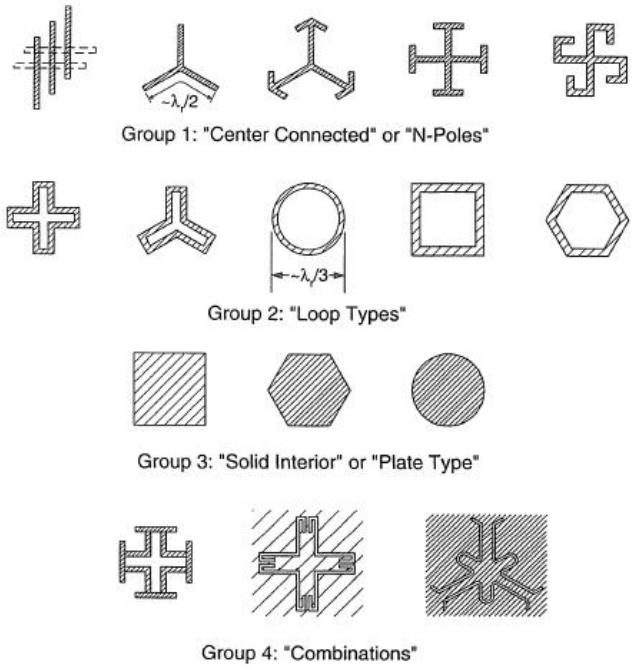

Figure 2.12: Typical element types arranged in groups [9]

2.4.1 Slot (Dipole) Types

The group of center connected elements (N-poles) include the simple straight element (dipole), three-legged element (also named as *tripole*), anchor element, Jerusalem cross and the square spiral. We will give most emphasis to the slot element since it is the Babinet complement of dipole element which is the basis for most of the other element types.

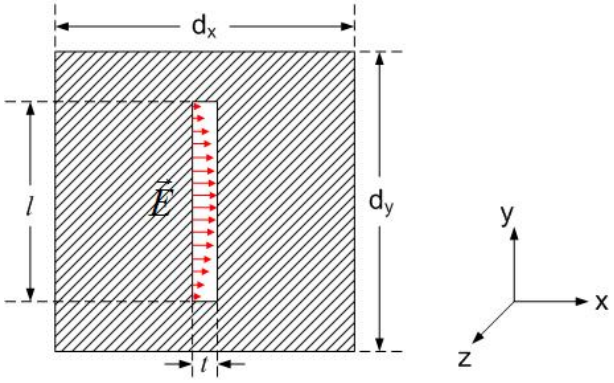

Figure 2.13: Unit cell of a slot FSS with electric field lines on the aperture

Similar to a dipole antenna, a dipole FSS resonates when the element is half-wavelength. By Babinet's principle, a slot FSS with slot length l has a resonant frequency around:

$$f_c = \frac{1}{2l\sqrt{\mu\epsilon}} \tag{2.3}$$

Effect of slot length on the resonant frequency is shown in Figure 2.14 for a free-standing single layer slot FSS. The resonant frequency shifts downwards as the length of slot is increased. Furthermore, the bandwidth can be increased to some extent by increasing the slot thickness. This is an expected result since it is well known from antenna theory that the bandwidth of a dipole generally increases with wire radius. The same is true for a slot (dipole) FSS as shown in Figure 2.15.

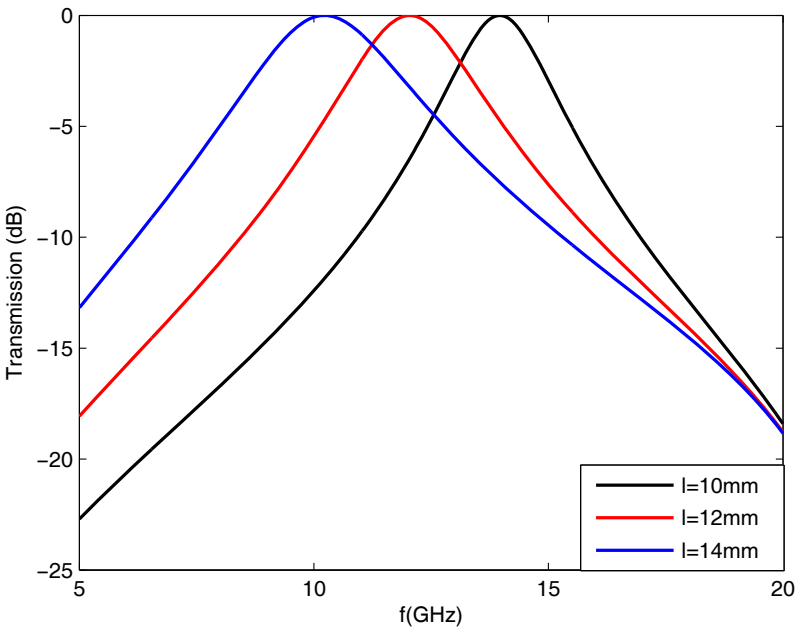

Figure 2.14: Variation of transmission with slot length ($d_x = d_y = 15mm$, $t = 1.2mm$)

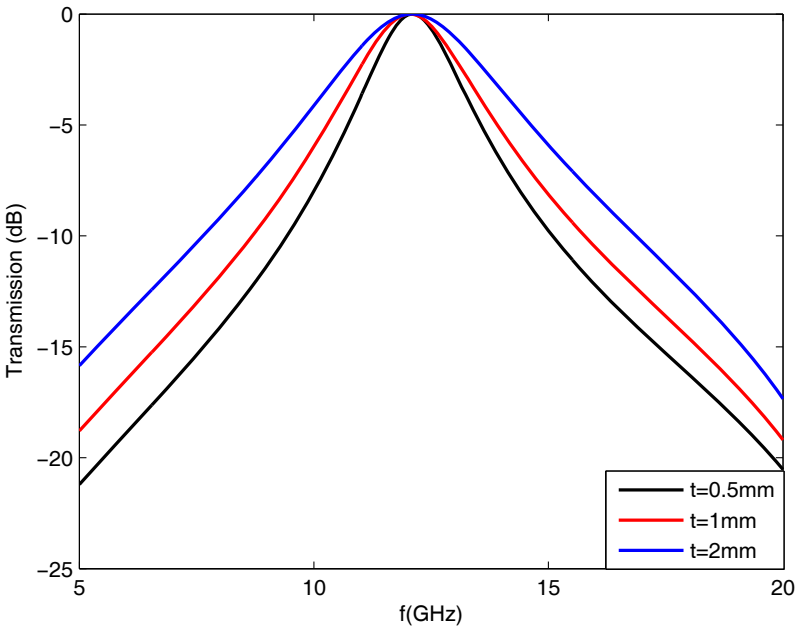

Figure 2.15: Variation of transmission with slot thickness ($l = 12mm$, $d_x = d_y = 15mm$)

Figure 2.16 shows the variation of transmission curves with inter-element spacings d_x and d_y. As a direct consequence of Floquet's theorem, the phases of the induced magnetic currents change with angle of incidence as indicated in (2.2). Furthermore, the mutual coupling between the elements decreases as we increase the inter-element spacings. However, large inter-element spacings will lead to early onset of *grating lobes*. Grating lobes are unwanted transmissions occuring when the phase delay between two neighboring elements equals a multiple of 2π [9]. Note in Figure 2.16 that the transmission curve for $d_x = d_y = 20mm$ has a grating lobe around 19.5GHz. In order to avoid early onset of grating lobes, the inter-element spacings must be chosen rather low. By this way, the bandwidth may also be enhanced as clearly seen in Figure 2.16.

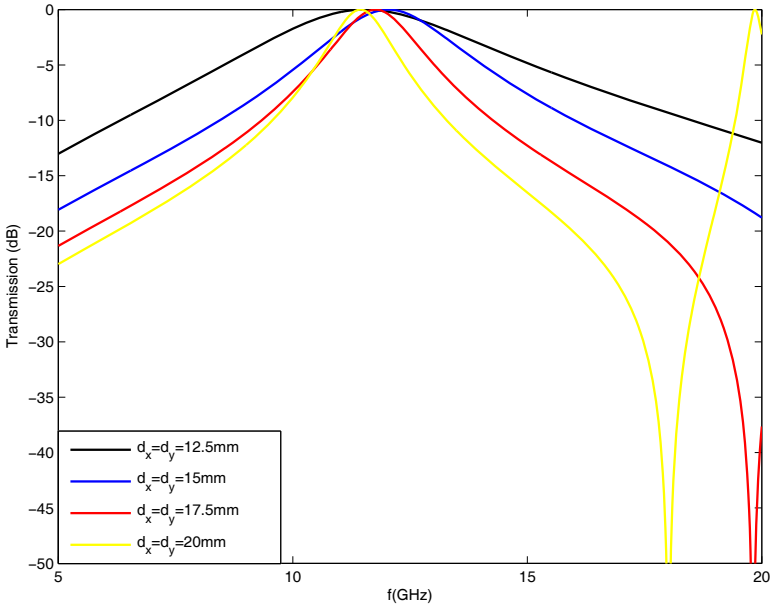

Figure 2.16: Variation of transmission with inter-element spacing ($l = 12mm$, $t = 1.2mm$)

2.4.2 Loop Types

The group of loop type elements are comprised of four-legged loaded element, three-legged loaded element, circular loop, square loop and hexagonal loop as seen in Figure 2.12 [9]. Among these elements square loop is the most suitable element to deal with because other elements (especially circular loop) will require more precise fabrication than square loop. Available mechanical etching techniques lose their precision for dimensions less than one-third of a millimeter and may cause significant discrepancies between simulated and measured results for circular or other type of loop elements.

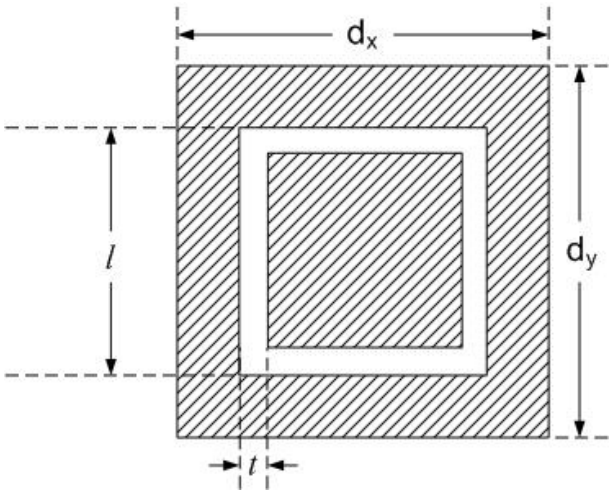

Figure 2.17: Unit cell of a loop FSS

The unit cell of a typical loop FSS is shown in Figure 2.17. The loop FSS is a polarization independent structure supporting both vertical, horizontal and circular polarizations.

The simplest way to figure out the working principle of a loop FSS is to consider the loop as a combination of an aperture ($l \times l$) loaded with a patch ($(l - 2t) \times (l - 2t)$) inside. For a vertically polarized incident electric field, the surface can be visualized as composed of infinitely long vertical rods leading to an inductive effect. The horizontal bars and patches inside the loops will act like capacitors in parallel with the inductors. At resonance we therefore obtain perfect transmission. The resonant frequency may be varied by tuning the edge length and thickness of the loop shown in Figure 2.18 and Figure 2.19.

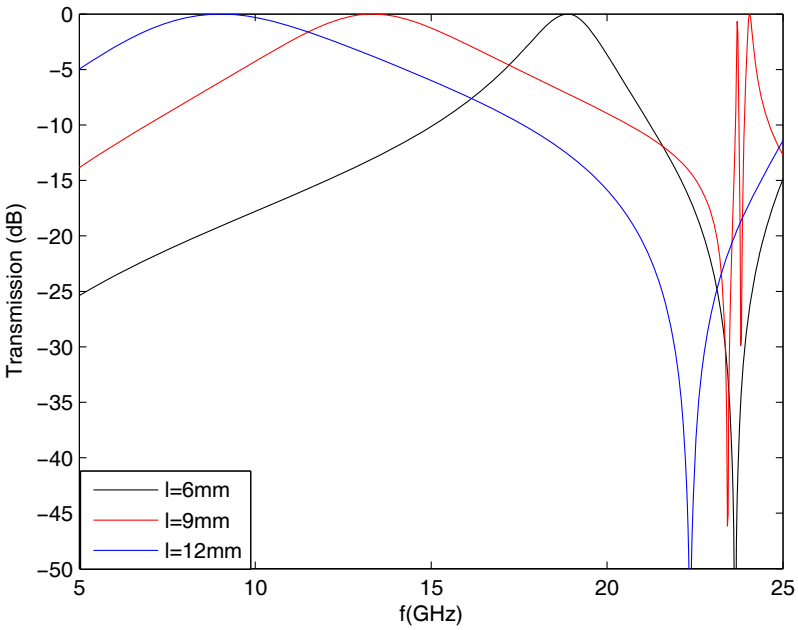

Figure 2.18: Variation of transmission with edge length of loop ($d_x = d_y = 15mm$, $t = 1.5mm$)

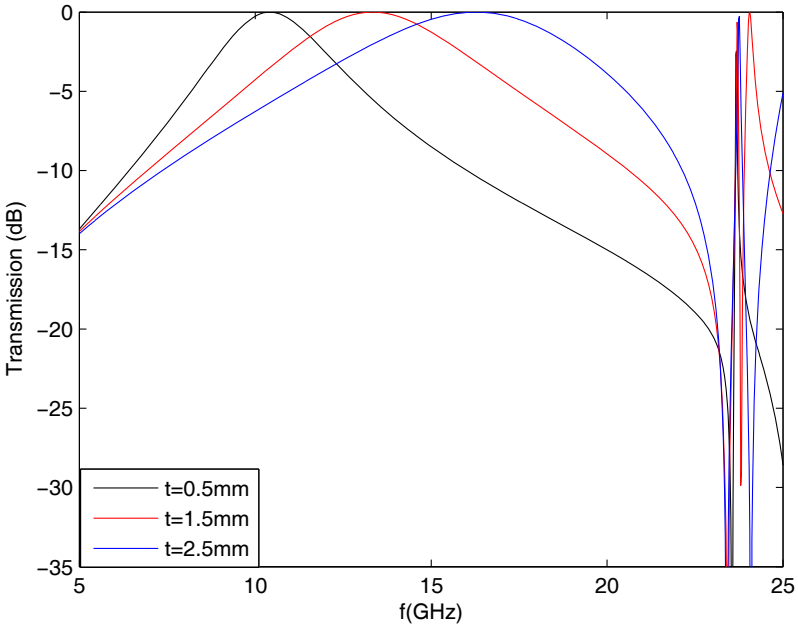

Figure 2.19: Variation of transmission with loop thickness ($l = 9mm$, $d_x = d_y = 15mm$)

Resonant frequency shifts downwards with increased edge length similar to the slot case. However, change of thickness has a completely different effect on slot and loop FSSs. It is concluded from Figure 2.19 that the resonant frequency increases when the thickness of the loop is increased. This result is evident when the FSS is envisioned as an equivalent LC network. The relevant conductors surrounding the loop and inside the loop act like a capacitor. When the thickness of the loop is decreased, these conductors come closer and the equivalent capacitance is boosted. Therefore, the resonant frequency moves down with increased capacitance.

Figure 2.19 also reveals that the grating lobes around 24GHz does not depend on loop thickness because they are only consequence of large inter-element spacings. For large inter-element spacings, the grating lobe occurs at a lower frequency because the phase delay between adjacent elements becomes a multiple of 2π. If the elements are brought closer, the onset of grating lobes can be pushed upwards as seen in Figure 2.20.

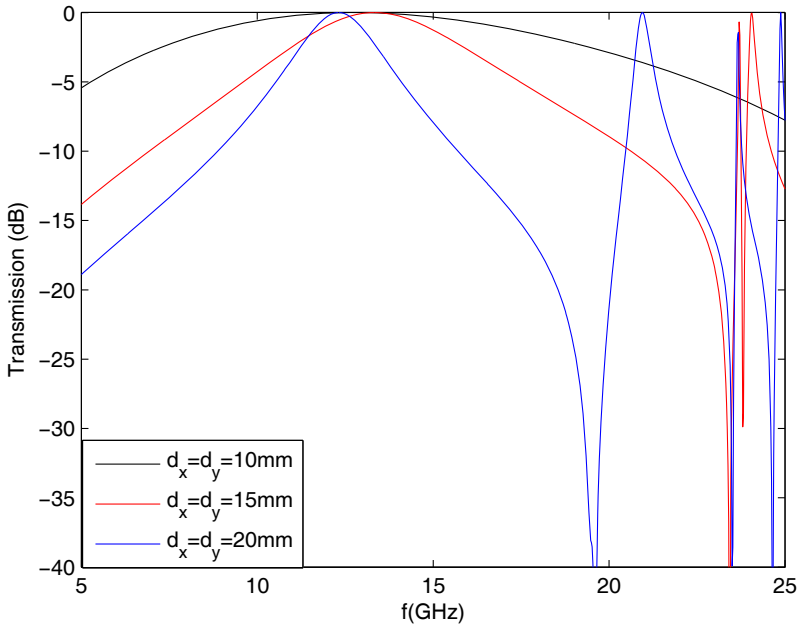

Figure 2.20: Variation of transmission with inter-element spacing ($l = 9mm$, $t = 1.5mm$)

2.4.3 Patch Types

This group of elements include plates of simple shapes such as squares, hexagons, circular disks for the reflecting case and their complementary geometries of apertures for the transparent case. This class of surfaces leads to element dimensions close to $\lambda/2$; that is, the inter-element spacing must be somewhat large leading to early onset of grating lobes for oblique angles of incidence. A square aperture can be viewed as a special case of square loop where the loop thickness is increased until there is no patch inside it. In that case the capacitance between the conductors will be very small due to large separations. A square aperture FSS without any loading can never resonate at the operating frequency of a loop FSS with same dimensions.

The patch (plate) types without any form of loading are the least favorite family of elements in FSS design due to their big geometries.

2.4.4 Comparison of Elements

Frequency responses of FSSs based on different unit element types are comparatively investigated. Slot element is studied in the sense that it will constitute a basis for other type of elements. The slot FSS resonates when the slots are half-wavelength and an incident electric field in the direction perpendicular to the slot is incident on the surface. The resonant frequency shifts downwards as the length of slot increases, and the bandwidth extends with thickness of the slot.

In the case of the loop FSS, for a vertically/horizontally polarized electric field, infinitely long rods between the adjacent loops act like an inductor. The gaps between the conductors surrounding the loop and inside the loop behave like a capacitor. Thus, the overall structure has an LC behavior having perfect

transmission at resonance. Similar to slot FSS, the resonant frequency of the loop FSS shifts downwards as the edge length of the loop increases. The bandwidth increases by increasing thickness as in the slot FSS case. However, the resonant frequency is not constant as in the slot case. Since the capacitance due to the gaps of the loop changes with thickness, the resonant frequency moves up when the thickness of the loop is increased.

The resonant frequency is almost constant when the inter-element spacing is changed in both FSS topologies. An important conclusion is that, large inter-element spacings lead to early onset of grating lobes, no matter what type of element. Therefore, a *quality* element must be small in terms of wavelength so that the inter-element spacing can be kept small. The size of the loop element is typically 0.3λ whereas the slot element is $\lambda/2$ long. The slot FSS in addition cannot offer as wide bandwidth as loop FSS can.

Chapter 3

Measurement of Dielectric Properties of Materials

3.1 Introduction

Every material has a unique set of parameters depending on its dielectric properties. A material is classified as 'dielectric' if it has the ability to store energy when an external electric field is applied [23], [24]. For an external electric field **E**, the electric displacement (electric flux density) is:

$$\mathbf{D} = \epsilon \mathbf{E} \tag{3.1}$$

where $\epsilon = \epsilon_0 \epsilon_r$ is the absolute permittivity, ϵ_r is the relative permittivity and $\epsilon_0 = \frac{1}{36\pi} \times 10^{-7}\ F/m$ is the free-space permittivity and **E** is the electric field.

Permittivity describes the interaction of a material with an electric field **E** and is a complex quantity:

$$\epsilon_r = \frac{\epsilon}{\epsilon_0} = \epsilon_r' - j\epsilon_r'' \tag{3.2}$$

The real part of permittivity (ϵ_r') is a measure of how much energy is stored in a material from an external electric field. The imaginary part of permittivity (ϵ_r'')

is the loss factor and a measure of how dissipative or lossy a material is to an external electric field. The imaginary part of permittivity (ϵ_r'') is always greater than zero and much smaller than the real part (ϵ_r'). The loss tangent or $\tan\delta$ is defined as the ratio of the imaginary part of the dielectric constant to the real part:

$$tan\delta = \frac{\epsilon_r''}{\epsilon_r'} = \frac{Energy\ Lost\ per\ Cycle}{Energy\ Stored\ per\ Cycle} \tag{3.3}$$

Analogous to permittivity, permeability (μ) describes the interaction of a material with an external magnetic field and is a complex quantity with real part (μ') representing energy storage term and imaginary part (μ'') representing the energy loss term. Relative permeability (μ_r) is the permeability relative to free space:

$$\mu_r = \frac{\mu}{\mu_0} = \mu_r' - j\mu_r'' \tag{3.4}$$

where $\mu_0 = 4\pi \times 10^{-7}\ H/m$.

Most of the materials in real life are non-magnetic, making the permeability very close to the permeability of free space. Materials exhibiting appreciable magnetic properties such as iron, cobalt, nickel and their alloys are some exceptions for this case; however, all materials, on the other hand, have dielectric properties, so the focus of this chapter will mostly be on permittivity measurements.

In this chapter, a comparative investigation of several material dielectric measurement techniques is provided in Section 3.2. Since the dielectric properties of a material are not constant and change with frequency, temperature, pressure, orientation etc; accurate modeling of these properties is crucial. Section 3.3 presents a more detailed explanation of the measurement setup we have constructed for the characterization of materials to be used in frequency selective surface (FSS) design.

3.2 Measurement Techniques

Accurate measurement of the dielectric properties of a material can provide scientists and engineers with valuable information to properly incorporate the material into its intended application for more solid designs or to monitor a manufacturing process for improved quality control.

A dielectric material measurement is worthwhile for providing critical design parameters for many electronics applications. For example, the impedance of a substrate, the loss of a cable insulator, the frequency of a dielectric resonator can be related to its dielectric properties. The information is also beneficial for improving absorber and radome designs. In this manner, the constitutive parameters of materials need to be measured accurately and characterized well throughout the design in order to minimize the discrepancies between the measurements and simulations.

The most commonly used dielectric measurement techniques include coaxial probe method, transmission line method, free-space method, resonant cavity method and the method of parallel plates [25].

3.2.1 Coaxial Probe Method

A coaxial probe dielectric measurement system seen in Figure 3.1 typically consists of a network or impedance analyzer, a coaxial probe (also called dielectric probe) and software. An external computer is needed to control the network analyzer through GP-IB cable. For the PNA family network analyzers of Agilent Technologies, the software can be installed directly in the analyzer and there is no need for an external computer.

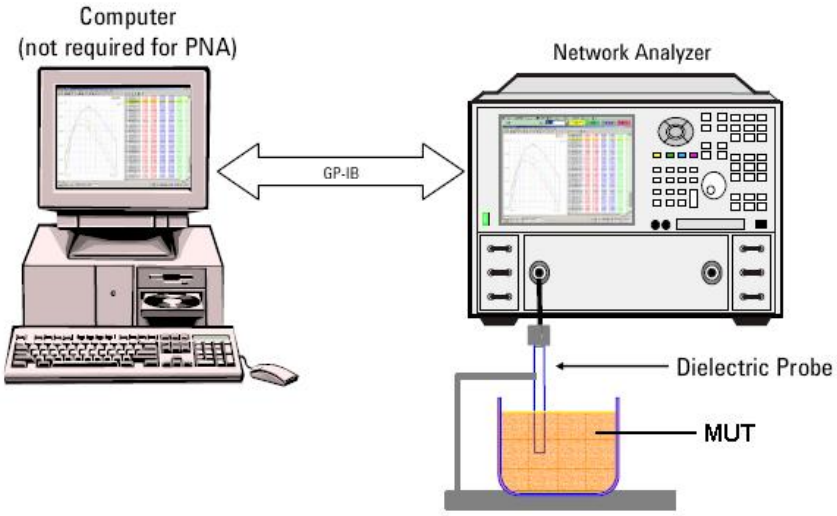

Figure 3.1: Coaxial Probe System [26]

The coaxial probe is a cut-off section of an open-ended transmission line. The material is measured by immersing the probe into a liquid or flanging it to the flat surface of a solid (or powder) material. The fields at the probe end penetrate into the material and change as they come into contact with the MUT (material under test). The reflected signal (S_{11}) is measured and related to ϵ_r [27].

The coaxial probe technique is best for liquids and semi-solids. It is convenient over a wide frequency range, from 200MHz up to 50GHz; however, it is not well suited to low loss or magnetic materials.

3.2.2 Transmission Line Method

A transmission line system consists of a network analyzer and a sample holder connected between the two ports of the analyzer. Transmission line method involves placing the material under test inside a portion of an enclosed transmission line. The transmission line is usually a section of rectangular waveguide or coaxial airline as seen in Figure 3.2. Permittivity and permeability

are calculated from the measurement of the reflected signal (S_{11}) and transmitted signal (S_{21}).

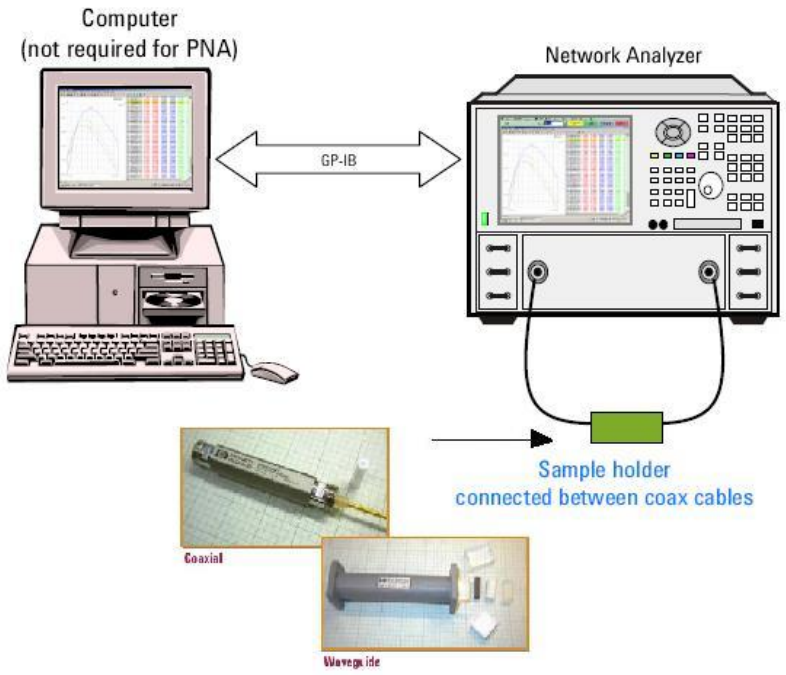

Figure 3.2: Transmission Line System and Samples [26]

Transmission line method is a broadband technique with high accuracy; however, it requires very precise machining of the material to fit the cross section of a coaxial or waveguide airline.

3.2.3 Free Space Method

A free space dielectric measurement system shown in Figure 3.3 consists of a network analyzer and the material positioned on a sample holder between two antennas facing each other.

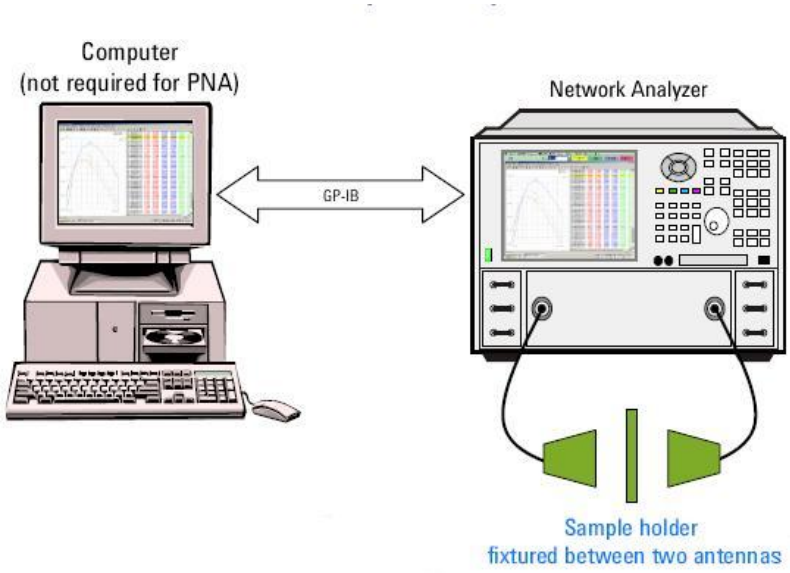

Figure 3.3: Free Space System [26]

The free space method uses two antennas to focus electromagnetic energy at a slab of material on a sample holder. Permittivity is calculated from the measurements of transmission through and/or reflection off the material.

Free space method is the most widely used non-contacting method among the dielectric measurement techniques. The free space method offers the advantage of the characterization of not only dielectric materials but also magnetic and anisotropic materials at microwave frequencies [28],[29]. The disadvantage of the free space method is the complexity of the free space calibration standards because they are 'connector-less'. Errors from diffraction effects at the sample edges and multiple reflections between antennas can reduce the accuracy of this method. These errors may be eliminated by use of a quasi-optical measurement systems in which optical lenses are used to focus the wave into a smaller section of the sample [30],[31]. Alternatively, advanced calibration techniques that will be explained in detail in Section 3.3.1 can be employed.

3.2.4 Resonant Cavity Method

A resonant cavity system shown in Figure 3.4 consists of a network analyzer and a resonant cavity connected between two ports of the analyzer with coaxial cables.

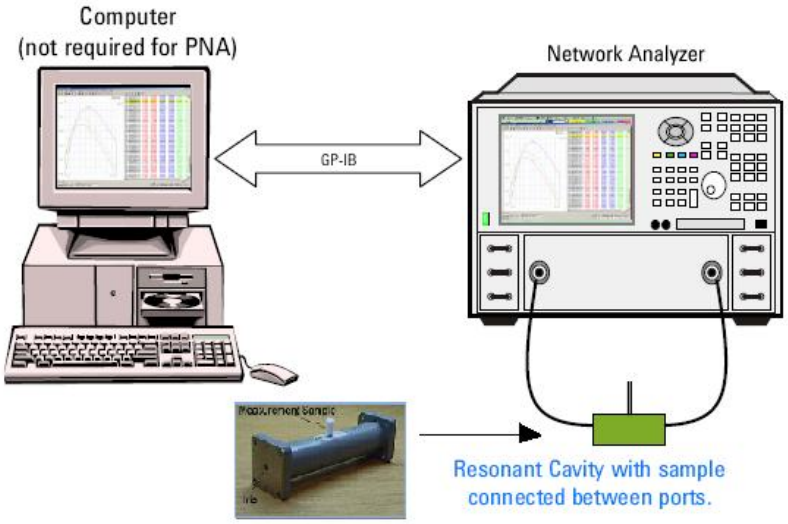

Figure 3.4: Resonant Cavity System [26]

Resonant cavities are high Q structures that resonate at a certain frequencies. A piece of sample material changes the center frequency (f_c) and the quality factor (Q) of the cavity. From these parameters, complex permittivity(ϵ_r) and complex permeability (μ_r) of a sample material with known physical dimensions can be calculated at a single frequency [24]. The most common application of this method is inserting a piece of sample through a hole on a rectangular waveguide [25]. For a permittivity measurement, the sample must be placed in a maximum electric field and for a permeability measurement in a maximum magnetic field. If the sample is inserted through a hole in the middle of the waveguide length, then an odd number of half wavelengths (n=2k+1) will bring the maximum electric field to the sample location, so that dielectric properties of the sample can be measured [32]. An even number of half wavelengths (n=2k)

will bring the maximum magnetic field to the sample location and the magnetic properties of the sample can be measured.

With its high accuracy, resonant cavity is the best method for very low-loss materials; however, it is still subject to errors. The network analyzer must have excellent frequency resolution to measure very small changes in the quality factor of the resonator [25]. The main disadvantage of resonant cavity method is the difficulty to precisely manufacture the samples.

3.2.5 Parallel Plate Method

The parallel plate capacitor method involves sandwiching a thin slab of material between two electrodes to form a capacitor. An LCR meter or impedance analyzer is used to measure the capacitance from which dielectric properties can be extracted. The parallel plate method is very accurate and typically used for frequencies lower than 1GHz [26].

3.3 Free Space Dielectric Measurement Setup

In this section, the free space dielectric measurement setup we constructed is explained in detail together with the measurement method, calibration techniques and measurement results.

In order to measure and characterize the dielectric properties of the materials to be used in FSS design, we assembled a free-space dielectric measurement setup as seen in Figure 3.5. The setup consists of an Agilent PNA series network analyzer, two X-band constant gain horn antennas, a sample holder and coaxial cables connecting the antennas to the ports of the network analyzer. There is no need for an external computer since the software is installed on the analyzer. The

antennas and the sample holder is placed on a metallic flat surface covered by absorbers. The antennas are aligned to transfer maximum power to each other.

Figure 3.5: Free Space Dielectric Measurement Setup

There are two important factors in determining the antenna type, distance between the antennas and the dimensions of the sample holder. Firstly, the electromagnetic waves radiated by the antennas should penetrate into the material as plane waves. To achieve this, the separation between the sample holder and each antenna should be large enough to satisfy the far-field criterion for the antennas. However, it has been observed by measurements that shorter distances can also yield accurate results. The optimum distance should be determined by trial and error. The other requirement is that, the sample holder should enclose the main beam of the antenna so as to minimize the reflections from the edges of the sample holder. Residual reflections are eliminated by absorber lining throughout the surfaces of the mounting plate and the sample holder. In addition to these; the sample holder must be parallel to the apertures of the antennas to ensure normal incidence of plane waves on the material.

3.3.1 Free Space Calibration

Calibration procedure for a free space measurement is challenging with respect to other measurement methods because the calibration standards are 'connector-less'. In addition to a conventional 2-port calibration, free space calibration must also be performed to shift the reference plane to the surface of the slab under test. For free space calibration, we use advanced Gated Reflect Line (GRL) calibration technique which is included in Agilent 85071E Material Measurement Software[33]. Before the GRL calibration, a full two-port calibration is performed at the end of the coaxial cables to be connected to antennas. The first step of the free space calibration is to find out the location of the sample holder in time domain. The rays diffracted from the edges of the sample holder travel more distance–thus spend more time– than the direct rays passing through the material. Therefore, the effect of these rays can be eliminated by applying a time domain gating which will ensure that we only deal with the direct rays passing through the material. The '*time domain*' function of the network analyzer is used to trace S_{11} as a function of time. S_{11} is traced both when the sample holder is empty and a metal plate exist on the sample holder. When these traces are compared, the reflected pulse from the metal plate can be observed and this gives the location of the sample holder in time domain (See Figure 3.6).

Once the location of the sample holder is determined, a time domain gating should be applied there in order to eliminate the reflections other than the material. There are four types of filters for gating: minimum, normal, wide and maximum–in the order of sharpness. The unwanted reflections are filtered out and this operation is called gating, corresponding to the word '*gated*' in GRL (Gated Reflect Line). In frequency domain, filters with sharp transition can cause ripples in band, whereas filters with smooth transition can be the source of distortion at the edges of the band while minimizing the in-band ripples. Filter

Figure 3.6: A typical S_{11} plot indicating the location of the sample holder in time domain

type must be chosen by considering the material type and measurement band. The normal type filter is selected for X-band material measurements. The gating width should be the same as the duration of the reflected pulse from the metal plate in time domain. In general, 1-2nsec gives the best results.

Having obtained the time domain gating parameters, a metal plate with flat surface and known thickness is placed on the sample holder, S-parameters are measured and stored by the software. This step corresponds to the word '*reflect*' in GRL. Then the metal plate is removed and same measurements are performed with empty fixture. This step is the '*line*' in GRL and the calibration process is completed.

There are several factors affecting the quality of the free space calibration. The most important is the beamwidth of the antennas and whether the sample holder encloses the main beam at all or not. Ideally, it is expected that the waves radiated by the first antenna should reach the other with no reflections. This is impossible in practice thus the reflections from the empty fixture should be minimized. To achieve this, antennas can be brought closer to each other with the necessity of the plane wave model in mind. A more expensive but accurate way is to use spot focussed lens horn antennas which can illuminate a small

portion of the material but not the edges of the sample holder [31]. In order to increase the quality of the calibration, we have covered the sample holder and supporting structure with wideband radar absorbing materials (RAM) which can effectively eliminate the reflections when backed by a metallic surface.

3.3.2 Measurements & Results

Having the free space calibration completed, the setup is ready for material measurements. The material with known thickness is fixed on the sample holder and the S-parameters are measured. The material parameters can be extracted using the relation between S-parameters and material properties that is given by the following set of equations [28]:

$$S_{21} = S_{12} = \frac{T(1-\Gamma^2)}{1-\Gamma^2 T^2} \tag{3.5}$$

$$S_{11} = S_{22} = \frac{\Gamma(1-T^2)}{1-\Gamma^2 T^2} \tag{3.6}$$

$$\Gamma = \frac{\gamma_0\mu - \gamma\mu_0}{\gamma_0\mu + \gamma\mu_0},\ T = e^{-\gamma d} \tag{3.7}$$

$$\gamma_0 = \frac{w}{c}\ ,\ \gamma = \frac{w}{c}\sqrt{\mu_r\epsilon_r} \tag{3.8}$$

where d is the thickness of the material under test, Γ is the reflection coefficient of the sample, T is the transmission coefficient through the sample, γ and γ_0 are the propagation constants in sample and free-space, respectively.

Agilent 85071E Material Measurement Software offers different methods according to the material type. If the material is known to be non-magnetic, only dielectric constant is calculated assuming the permeability of the material is the same as free space permeability. This method gives the most accurate results for non-magnetic materials. Another method is the 'Nicholson-Ross Model' which gives the best results for magnetic materials by calculating all the material properties.

Measured dielectric constants for RO4003C® high frequency laminate of Rogers Corporation [37] and ROHACELL® HF-71 foam along the X-band are shown in Figure 3.7 and Figure 3.8, respectively.

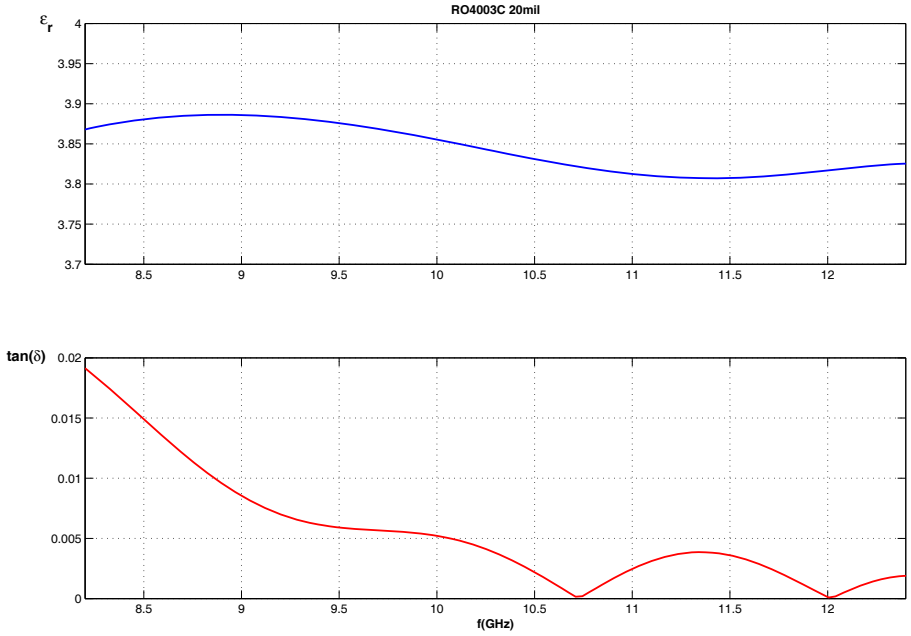

Figure 3.7: Dielectric constant and loss tangent of RO4003C® Laminate

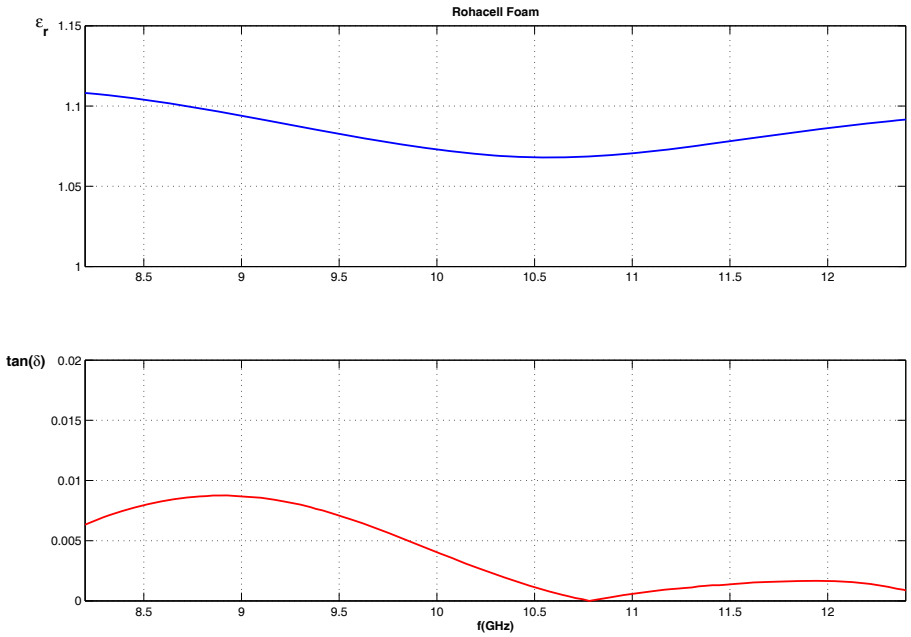

Figure 3.8: Dielectric constant and loss tangent of ROHACELL® HF-71 Foam

Rogers Corporation states the dielectric constant (ϵ_r') of RO4003C® as 3.38 ± 0.05 and the loss tangent as 0.0035 maximum at 10GHz [37]. They do not declare that the results shown on the data sheet will be achieved by a user for a particular purpose. The suitability of the material for a specific application is left to the user. In the free space dielectric measurement setup, the dielectric constant (ϵ_r') of RO4003C® is measured as 3.85 ± 0.05 and the loss tangent is around 0.005 at 10GHz. The measured dielectric constant of ROHACELL® HF-71 foam agrees well with the one specified in the data sheet except for the loss tangent.

The measurement results of complex parameters (ϵ_r'')–thus loss tangents– are not as accurate as real parameters (ϵ_r') because the materials under test are low-loss materials and free space method does not offer high resolution in the measurement of the imaginary part of the permittivity. However, we obtain repeatable and reasonable results by cascading more than one slab, namely increasing the thickness of the material under test and thus the overall loss. These values are used as inputs to the design of dielectric loaded FSS in the following chapter.

Chapter 4

FSS Radome Design and Measurements

4.1 Introduction

In this chapter, the comparative investigation of slot and loop type FSSs presented in Section 2.4 is employed for the design of hybrid FSS radomes. The dielectric measurement results obtained in Chapter 3 are utilized throughout the design process. Three types of hybrid FSS radomes operating at X-band are designed and fabricated. Two of them are slot FSSs with different inter-element spacing and slot length, and the other is a modified loop type FSS what we call *single polarized loop FSS*. A conventional loop FSS is modified in such a way that one of the polarizations is eliminated because the antenna for which the radomes are designed is single polarized.

In Section 4.2 and Section 4.3, slot and single polarized loop FSS designs are given together with simulations supported by measurement results, respectively. Section 4.4 provides a comparison of frequency responses of the slot and the

single polarized loop FSSs in terms of the resonant frequency, bandwidth and sharpness of the transition from pass-band to stop-band.

4.2 Slot FSSs

The design of the two hybrid slot FSS radomes with different inter-element spacings has been presented in this section. Being the basis for most of the band-pass FSSs, slot FSS is chosen to be investigated in detail. It has been demonstrated in Section 2.4.1 that a single layer slot FSS resonates when its length is approximately half-wavelength. The bandwidth of the transmission curve depends on both the thickness of the slot and the inter-element spacings as explained before.

In this manner, double-layer slot FSSs with different inter-element spacings have been designed to operate at a center frequency f_1 with different bandwidths. Note that the center frequency f_1 is a frequency at X-band, and in this work it is not given explicitly because of being company confidential information for Aselsan Inc. The electrical spacing between the FSS layers is chosen to be around $\lambda/4$ for the best filter curve as suggested in Section 2.3.1.

4.2.1 Fabricated Prototypes

Two different slot FSSs are fabricated as shown in Figure 4.1. These two slot FSSs, whose unit cell dimensions are given in Table 4.1, are labeled as *Slot FSS-1* and *Slot FSS-2* to avoid confusion. For both FSS topologies, two FSS layers are sandwiched between three dielectric slabs. The dielectric profile shown in Figure 4.2-left is the same for all FSS radomes throughout this work.

	d_x (mm)	d_y (mm)	l (mm)	t (mm)
Slot FSS-1	13	13	11.5	1.2
Slot FSS-2	15	15	11.7	1.2

Table 4.1: Unit cell dimensions of the two slot FSSs

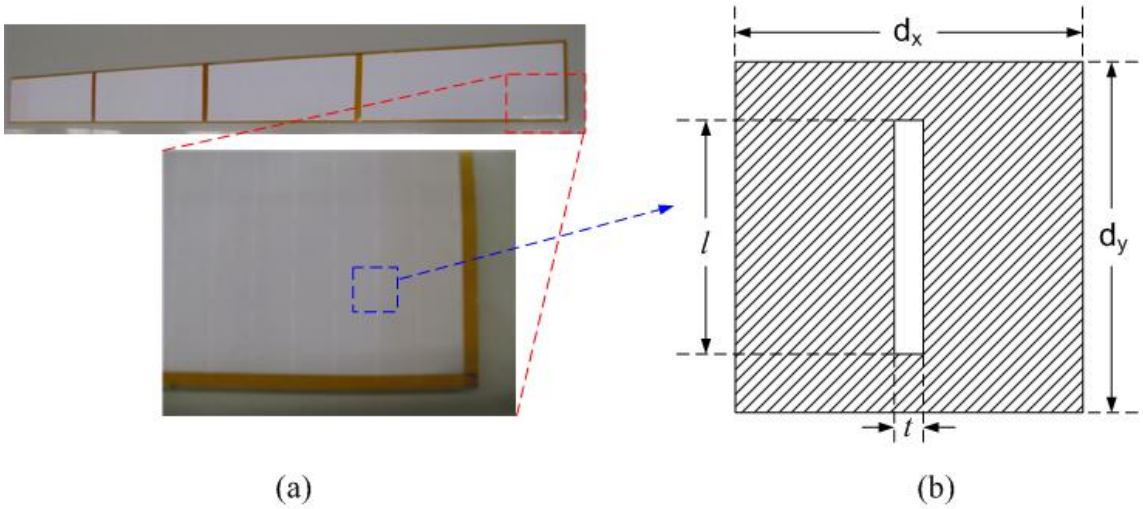

Figure 4.1: Fabricated hybrid slot FSS radome; (a) Front view, (b) Geometry of the unit cell

In the fabrication process, chemical etching technique with photolithography has been employed. The slot FSSs have been implemented on a RO4003C® high-frequency laminate, which is commercially available from Rogers Corporation. Low dielectric loss of this laminate facilitates its use in many applications where higher operating frequencies limit the use of conventional circuit board laminates [37]. The copper cladding on the unetched side of the laminate has been dissolved by chemical etching procedure. By this way, we have obtained thin FSS sheets of slot elements with dielectric slabs on one side. These FSS sheets are carefully aligned face to face with dielectric slabs on the other sides as shown in Figure 4.2 right. A 7.5mm thick ROHACELL® HF-71 foam is used between the FSS sheets to support them. The dielectric properties of both the outer and inner dielectric materials have been measured in free-space dielectric measurement setup as presented in Section 3.3.2. The measured

dielectric parameters and other relevant dimensions are given in Table 4.2 for RO4003C® laminate and ROHACELL® HF-71 foam.

	Intermediate slab	Outer slabs
Material	ROHACELL® HF-71	RO4003C®
Relative dielectric constant	1.075	3.85
Slab thickness (mm)	7.5	0.508
Thickness of the copper cladding (μm)	NA	35
Loss tangent	<0.005	<0.005

Table 4.2: Dielectric slab properties

The precise alignment of FSS sheets in line has utmost importance since transmission loss at resonance may occur if the two arrays are displaced [6]. By use of EM transparent adhesive tapes, sandwich structures shown in Figure 4.2 right have been stuck together and the resulting hybrid radome of Figure 4.1 is obtained. The resulting radome is 8.5mm thick with length $l = 204cm$ and height $h = 21cm$. Note that this procedure has been performed for both slot FSSs and eventually two radomes have been fabricated. The slot FSS-1 radome and slot FSS-2 radomes have been constructed from double layer arrays of 2496 and 1904 unit elements, respectively.

4.2.2 Measurements & Simulations

Numerical calculations of the transmission curves for the FSS radomes have been performed by CST Microwave Studio®, which is a full-wave 3D electromagnetic solver [36]. Rather than the whole FSS array, only the constituting unit cell is simulated by means of unit cell simulation as explained in Section 2.2. The fabricated radome prototypes have been measured in free space measurement setup shown in Figure 4.3. This setup consists of:

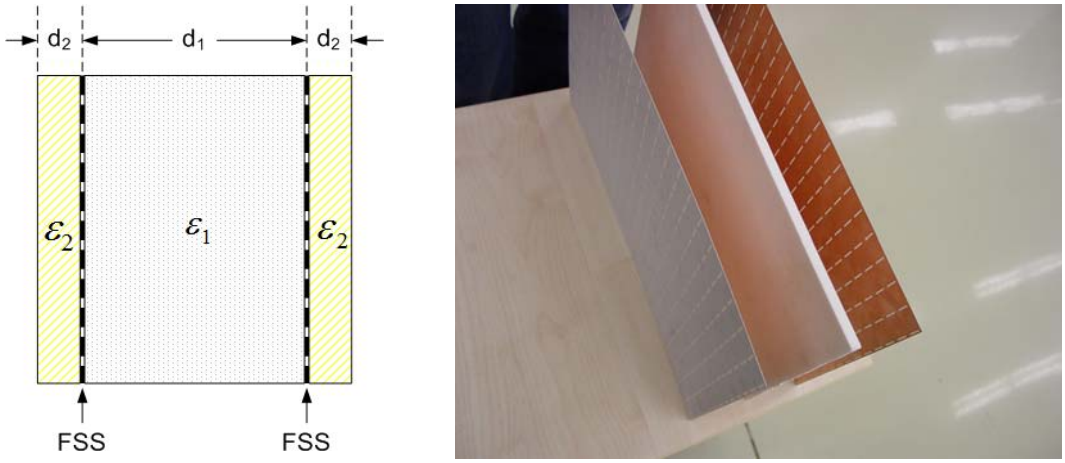

Figure 4.2: Dielectric profile for hybrid FSS radomes; *Left*: Cross-section with $d_1 = 7.5mm$, $\epsilon_1 \approx 1.075$, $d_2 = 0.508mm$, $\epsilon_2 \approx 3.85$, *Right*: Sandwiching the layers

- Agilent Technologies PNA series N5230A vector network analyzer,
- 2 constant gain X-band (8.2-12.4GHz) horn antennas,
- a sample holder,
- 50 Ω coaxial cables connecting antennas to network analyzer,
- and wideband RF absorbers.

Figure 4.3: Free Space Transmission Measurement Setup

Measuring the frequency response of FSSs is challenging when compared to that of a classic microwave filter. Scattering parameters of a microwave filter

can be measured by simply connecting it to the ports of a network analyzer after a two-port (or thru) calibration. Transmission response measurement of an FSS involves challenges such as multipath reflections and edge diffractions in the system. When these ray components are combined with the direct rays passing through the FSS sample, the resulting transmission curve may be extremely oscillatory with unwanted ripple levels. Agilent PNA series vector network analyzer offers time domain option which allows the user to make transformations between the frequency and time domains. In order to overcome the undesired reflections in the system, time domain gating has been employed throughout the measurements. By doing so, the rays which travel longer durations than the direct rays have been eliminated. Once the unwanted reflections in the system have been eliminated by applying a gating window in time domain, the transmission curves are smooth and *'ripple-free'*. The duration of the gating window in time domain should be chosen carefully. For this purpose, a thin planar metal plate is placed on the sample holder and S_{11} is plotted in time domain. The width of the reflected signal from the metal plate determines the duration of the gating window to be applied. If this duration is much more than it should be, then there will be ripples in the frequency domain transmission curve. On the other hand, a very narrow gating window will lead to a very smooth transmission curve with reduced accuracy and errors at frequencies close to the edges of measurement band. Measured and simulated transmission curves for slot FSS-1 and slot FSS-2 are presented in Figure 4.4 and Figure 4.5, respectively. The simulations are performed between 5-15GHz whereas the measurements are done between at X-band because the antennas are operating at X-band and measurement system is designed for this frequency band. Measurements of both FSSs are carried out with time domain gating. Figure 4.5 additionally shows the transmission curve measured without gating for comparison purposes.

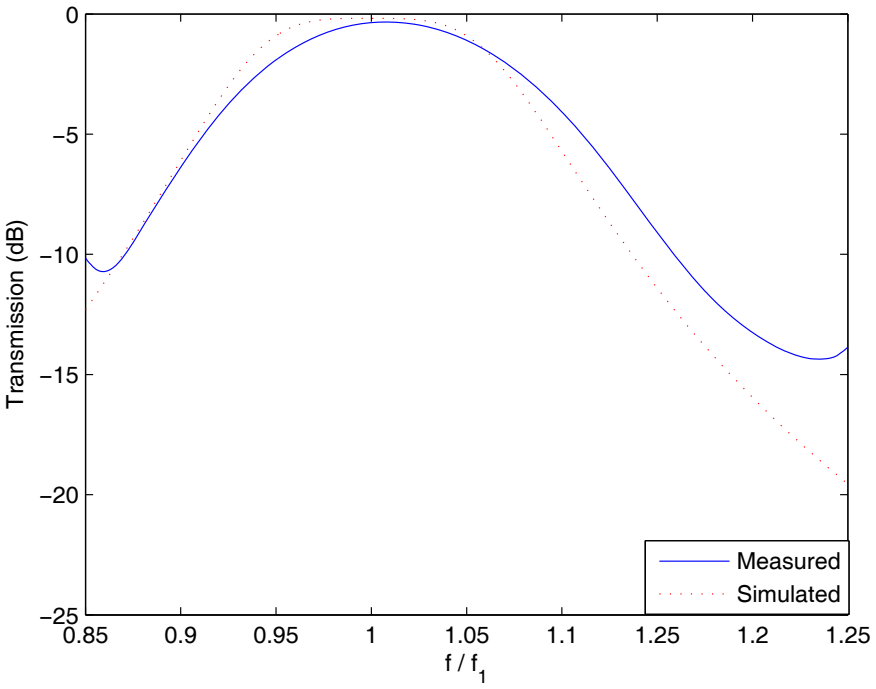

Figure 4.4: Measured and simulated transmission curves for slot FSS-1

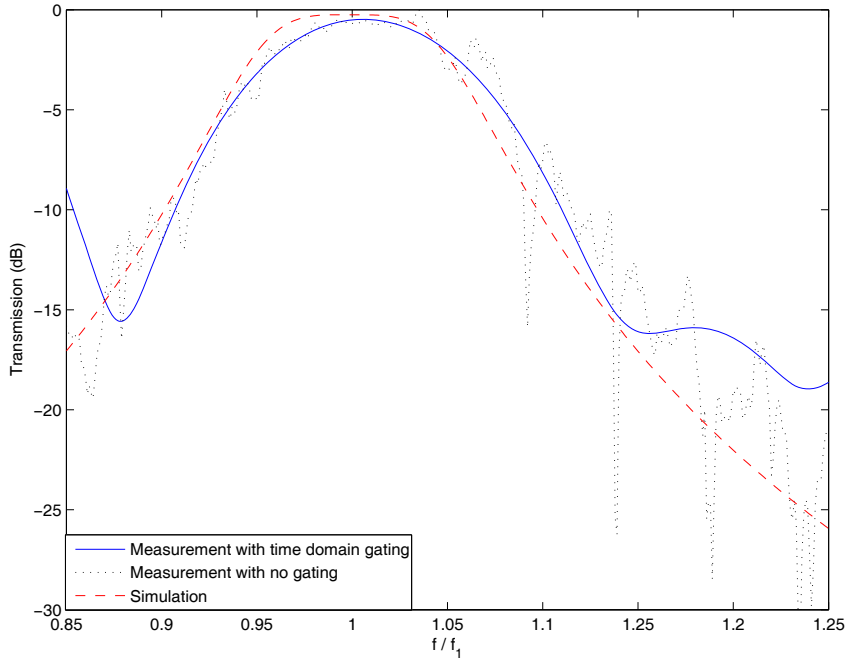

Figure 4.5: Measured and simulated transmission curves for slot FSS-2

Frequency selective nature of the fabricated prototype radomes is evident from the behavior of the transmission curves with resonant frequencies around f_1. It is obvious from both figures that quite good agreement is achieved between the numerical and experimental results. For both FSSs, measured transmission curves are smoother than simulated ones. This is an expected result of time domain gating which is applied to avoid unwanted reflections in the system as mentioned before. The inconsistency between numerical and experimental results at frequencies around the edges of measurement band evolves from the time domain gating. The measurement of slot FSS-2 without any gating proves this statement in the way that numerical and experimental result coincide well around the band edges as well. Out of band rejection around $1.25f_1$ is more than 25dB for both simulation and measurement of slot FSS-2. Slot FSS-1 has a wider bandwidth compared to slot FSS-2. This is simply because inter-element spacing of slot FSS-1 is smaller ($d_x = d_y = 13mm$) than that of slot FSS-2 ($d_x = d_y = 15mm$). Slot FSS-1 has a 0.5dB bandwidth of 9.5%, whereas slot FSS-2 has 7.2% bandwidth. As a consequence of this, the maximum out of band rejection offered by slot FSS-1 ($\sim$20dB) is smaller than offered by slot FSS-2 ($\sim$25dB). Note that the resonant frequency for both FSSs is around f_1 since the slot elements have approximately the same length.

4.3 Single Polarized Loop FSS

In this section the design of a single polarized loop FSS radome is presented. Single polarized loop FSS is a slightly modified version of conventional loop FSS. An ordinary square loop FSS, as mentioned in Section 2.4.2, is a polarization independent structure exhibiting wider bandwidth than slot FSSs. The antenna, which will be covered with FSS radome for RCS reduction, is a horizontally polarized slotted waveguide array (SWGA) antenna. FSS radome must be transparent at the operating frequency of the antenna and opaque at other

threat radar frequencies and polarizations. Therefore, the conventional loop FSS is modified to resonate only for horizontally polarized incoming waves and reject vertically polarized waves. In addition to frequency selectivity, the single polarized loop FSS has the function of polarization selectivity. Similar to the slot FSS case, the center frequency of the single polarized loop FSS at X-band will be denoted as f_2.

4.3.1 Modifications in Conventional Loop FSS

The conventional loop element has been modified in order to obtain a polarization selective surface. Due to the geometry of the square loop, it supports both vertical and horizontal polarizations. The electric field distribution on the loop is shown in Figure 4.6 for a vertically polarized incident plane wave. By duality, this distribution can also be envisioned as fictitious magnetic current distribution.

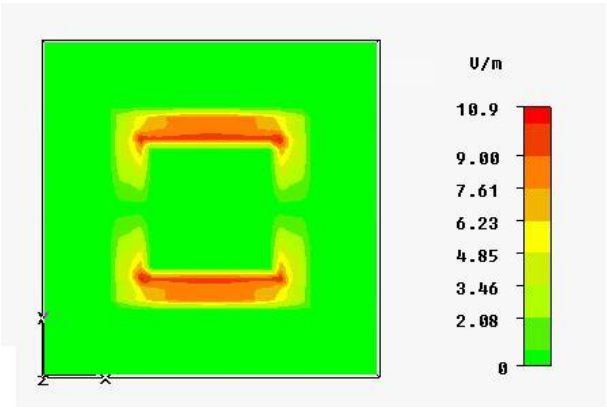

Figure 4.6: Electric field distribution on the square loop FSS at resonance

If a perfectly conducting thin strip is placed at the position where the electric field is maximum, the capacitive effect between the pertinent conductors can be removed. We have canceled out the capacitance by shorting the adjacent conductors in the vertical direction as shown in Figure 4.7.

We call the thin conducting strips '*polarization cancelers*' as they cancel out the vertical polarization component of the incident electric field by removing the

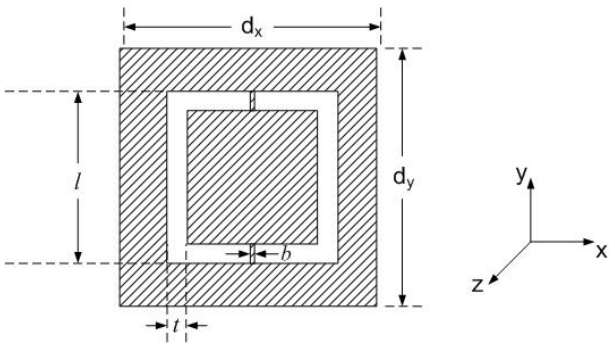

Figure 4.7: Unit cell of the single polarized loop FSS: vertical polarization is eliminated by thin strips of thickness $b = 0.2mm$. Other dimensions are $d_x = d_y = 15mm, l = 9mm, t = 1.5mm$

capacitance between the vertical conductors. The effect of these polarization cancelers on transmission is shown in Figure 4.8 for both co- (horizontal) and cross-polarizations (vertical) for single layer unloaded FSSs.

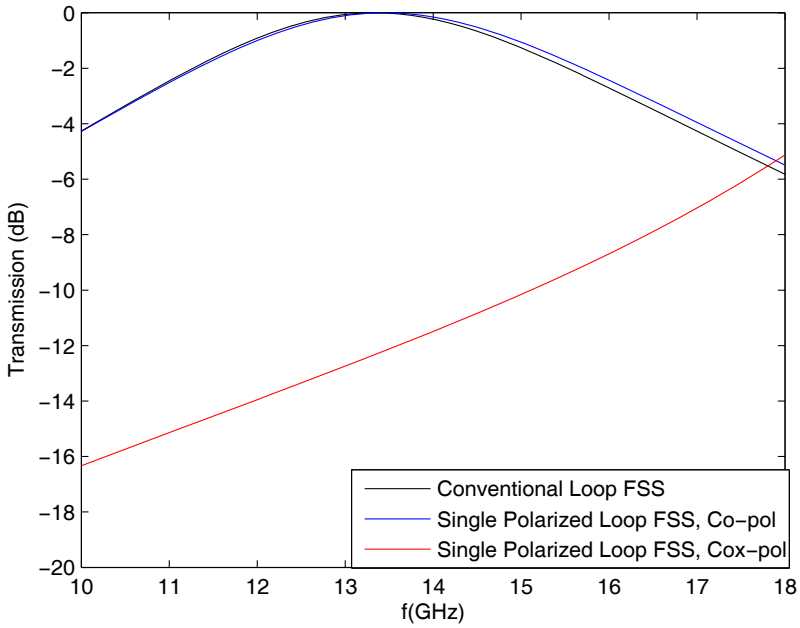

Figure 4.8: Effect of polarization cancelers on transmission for co- and cross-polarizations

It is evident from Figure 4.8 that vertical polarization is eliminated whereas horizontal polarization is not affected. The transmission curves for conventional loop FSS and modified single polarized loop FSS coincide very well for horizontal polarization. The cross polarization rejection is about 12dB at resonance for

single layer case; however, it will be shown in Section 4.3.3 that polarization rejection level around 25dB can be achieved for double layer FSS case.

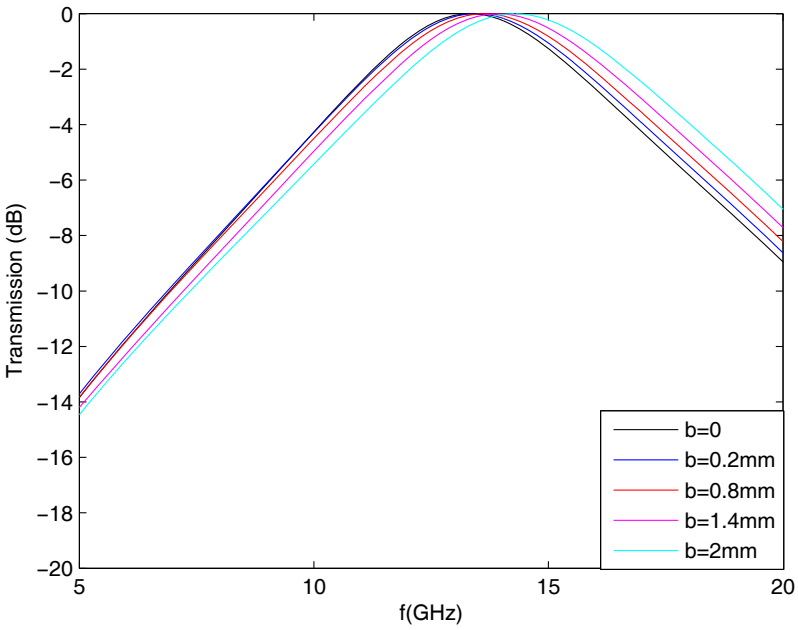

Figure 4.9: Variation of transmission with polarization canceler thickness b ($d_x = d_y = 15mm$, $l = 9mm$, $t = 1.5mm$)

Figure 4.9 shows that polarization canceler thickness does not have a significant effect on transmission curve. There is a slight shift upwards in the resonant frequency when the thickness is increased.

4.3.2 Fabricated Prototype

The single polarized loop FSS is fabricated as shown in Figure 4.10 with the unit cell dimensions given in the caption. Two FSS layers are sandwiched between three dielectric slabs. The same dielectric profile of slot FSSs shown in Figure 4.2 left is applied. The fabrication is implemented exactly in the same way as in slot FSSs case. The fabricated radome prototype is 8.5mm thick with length $l = 204cm$ and height $h = 21cm$.

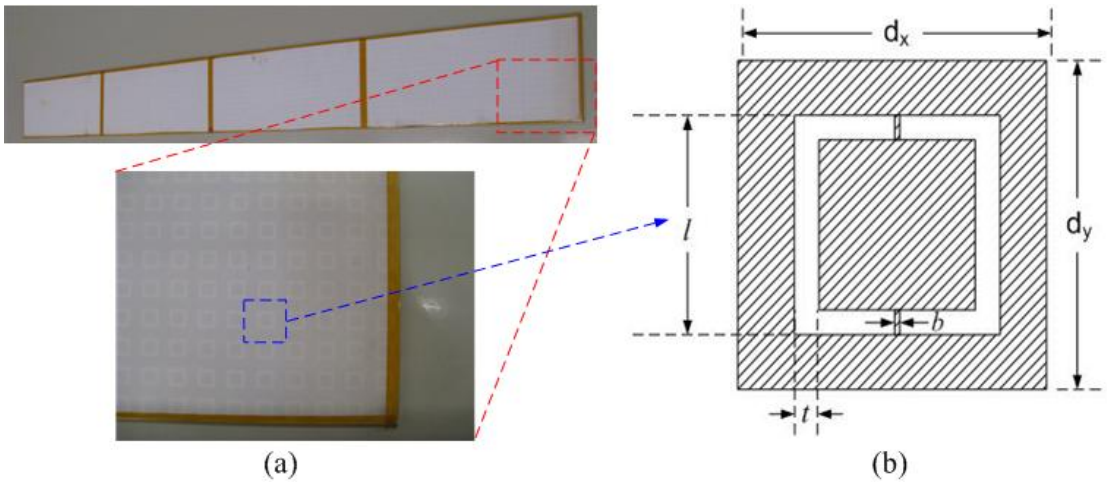

Figure 4.10: Fabricated single polarized loop FSS radome; (a) Front view, (b) Geometry of the unit cell: $d_x = d_y = 15mm$, $l = 9mm$, $t = 1.5mm$, $b = 0.2mm$

4.3.3 Measurements & Simulations

The transmission coefficients of the single polarized loop FSS radome for both polarizations are obtained by unit cell simulation in CST Microwave Studio®. The fabricated radome prototype has been measured in the free-space measurement system shown in Figure 4.3 with the same calibration settings as in slot FSS measurements.

Numerical and experimental transmission curves are presented in Figure 4.11 for both horizontal and vertical polarizations. Very good agreement is obtained between the simulated and measured results. The passband extends from $0.9f_2$ to $1.1f_2$ with f_2 being the center frequency. Note that the center frequency of the single polarized loop FSS is slighty larger than that of slot FSSs ($f_2 = 1.05f_1$). The measured resonant frequency is shifted $0.01f_2$ upwards compared to the simulated one. The measured 0.5dB bandwidth of the FSS radome is slightly narrower than the simulated bandwidth. Cross polarization level is approximately -25dB around the resonance. Undesired polarization component of the incident signal can be suppressed about 25dB at the center frequency. This clearly shows that the single polarized loop FSS radome is also a polarization selective structure. Simulated and measured insertion loss levels in the passband

coincide well, too. Minor discrepancies can be attributed to tolerances in the fabrication process, possible errors in the measurement due to time domain gating and fringing effects at the edges of the FSS radome.

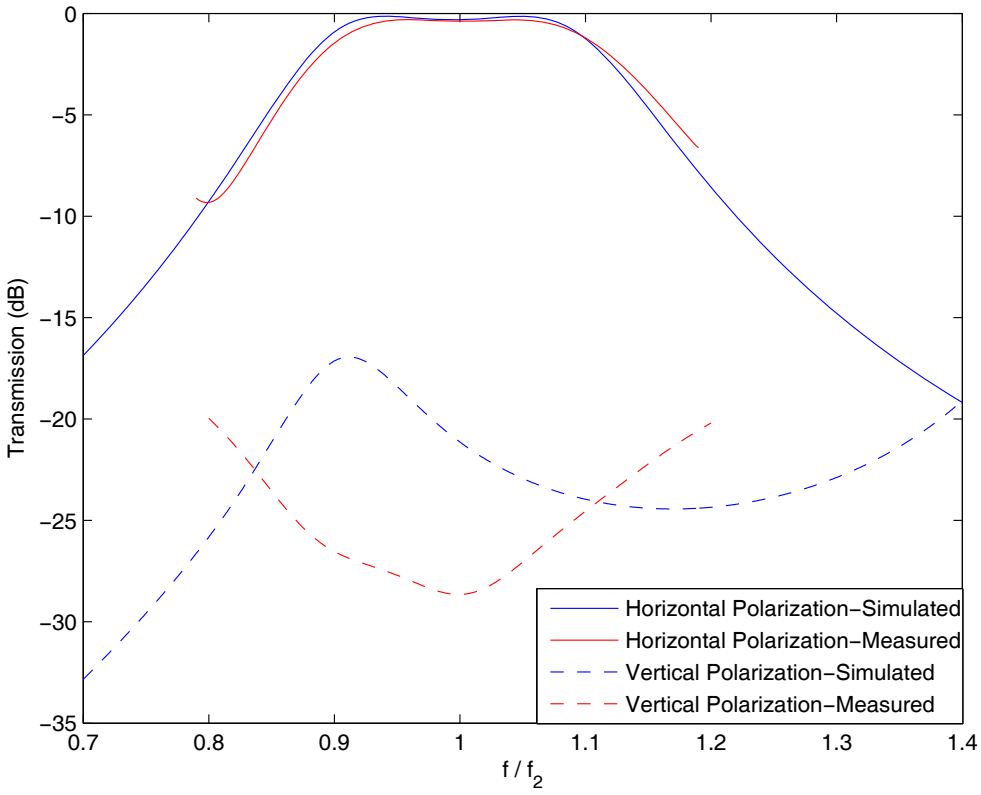

Figure 4.11: Measured and simulated transmission curves for single polarized loop FSS

4.4 Discussions on the Mentioned FSS Topologies

Throughout this chapter, three different hybrid FSS radomes have been designed, fabricated and their frequency responses have been studied both numerically and experimentally. Two of these radomes are based on slot FSSs and the third one utilizes a modified single polarized loop FSS unique to this work. In the case of all three radomes, the bandpass behavior of slot and modified loop FSSs can be observed in the vicinity of the resonant frequency. The two slot FSSs,

		Simulated	Measured
Slot FSS-1	Center Frequency	f_1	$1.01f_1$
	BW	9.5%	7.3%
	Loss (dB max.)	0.18	0.33
Slot FSS-2	Center Frequency	f_1	$1.01f_1$
	BW	7.4%	5.2%
	Loss (dB max.)	0.24	0.45
Single Polarized Loop FSS	Center Frequency	f_2	$1.01f_2$
	BW	18.9%	15%
	Loss (dB max.)	0.31	0.39

Table 4.3: Simulated and measured frequency characteristics of investigated FSS topologies

which have slot elements of approximately the same length, resonate at the center frequency of f_1. Their center frequencies are measured to be $1.01f_1$ for both. Slot FSS-1 has a wider bandwidth than slot FSS-2 because inter-element spacings are smaller than that of slot FSS-2. Due to closer inter-element spacings, slot FSS-1 exhibits a stronger resonance and has a transmission loss (0.18dB) less than slot FSS-2 has (0.24dB). The simulated and measured center frequencies, 0.5dB bandwidths and transmission losses of all FSS topologies are given in Table 4.3. The measured bandwidths of the slot FSS-1 and slot FSS-2 are %2.2 narrower when compared with the simulated bandwidths. For all FSS structures, the difference between the simulated and measured center frequencies are %1. When the single polarized loop FSS is compared with the slot FSSs, it is evident that the loop FSS has a broader bandwidth than both slot FSSs. Its bandwidth extends nearly to 15% whereas slot FSS-2 with the same inter-element spacings have a percentage bandwidth of almost one-third of that. However; slot FSSs, which are narrow banded when compared to loop FSS, offer deeper out of band rejection. For example, the slot FSS-2 has a rejection level more than 25dB at $1.25f_1$, whereas the rejection level of the loop FSS at the same frequency ($1.2f_2$) is only

around 10dB. The same comparison can be made between slot FSS-1 and slot FSS-2. Rejection levels of slot FSS-1 and slot FSS-2 are about 20dB and 25dB, respectively. Analogous to microwave filter theory, there is a trade-off between bandwidth and sharpness of transmission curves of frequency selective surfaces. Optimum element type and inter-element spacing must be determined according to the requirements of the application. In our case, all the fabricated radome prototypes can cover the operating band of the antenna with a transmission loss below 0.5dB.

Chapter 5

Radiation Pattern Measurements

5.1 Introduction

In literature, integration of an antenna with a frequency selective surface has been first reported in [17] to the best of our knowledge. In that work, Erdemli *et al.* utilized FSS to enhance antenna radiation efficiency for its high impedance characteristic like an artificial magnetic conductor. In addition, multilayer FSS structures combined with open-end waveguide radiators have been presented in [18]-[20]. However, they investigated only the filtering performance of the integrated module. In contrast to them, in this chapter we will present the radiation pattern measurements of a slotted-waveguide antenna with and without FSS radome prototypes in addition to free-space transmission measurements of the last chapter. The radiation pattern measurements presented in this chapter are conducted in the near-field antenna test range of Aselsan Inc.

Section 5.2 gives a brief description of the near-field test range with the basic idea behind near-field antenna measurement. Measured E- and H-plane radiation patterns of the antenna with/without FSS radome prototypes are presented in Section 5.3 and Section 5.4, respectively. Note that E-plane corresponds to

the azimuth and H-plane corresponds to the elevation cuts for the horizontally polarized antenna. Finally, discussions on the measurement results are provided in Section 5.5.

5.2 The Near-Field Test Range

The slotted-waveguide array antenna to be covered with FSS radome is a fan-beam antenna with a largest dimension of D about 1 meter. The Fraunhofer distance or the far-field distance, d, is considered to be;

$$d = \frac{2D^2}{\lambda} \tag{5.1}$$

where D is the largest antenna dimension and λ is the wavelength. Separating the antenna under test (AUT) and the source antenna by this distance reduces the phase variation across the AUT enough to obtain a reasonably good antenna pattern. The Fraunhofer distance of the slotted waveguide antenna, d, is above 100 meters for a frequency at X-band (24mm $< \lambda <$ 36mm). An anechoic chamber of this size does not exist; instead, a near-field antenna test range is used for this type of measurements.

The near-field antenna test range is a very compact and advanced antenna measurement facility (See Figure 5.1). Near-field measurements are conducted by scanning a small probe antenna over a planar surface. The AUT is fixed on a stationary mount and a near field probe, a short distance from the AUT, is moved along a flat surface. The collected near-field data is transformed to a far-field antenna pattern by use of a Fourier transform. Not only antenna patterns but also antenna polarization errors, directivity and antenna gain can be measured with this system. Antenna measurements within frequencies ranging from 0.8GHz up to 50GHz can be conducted with the aid of several near field measurement probes.

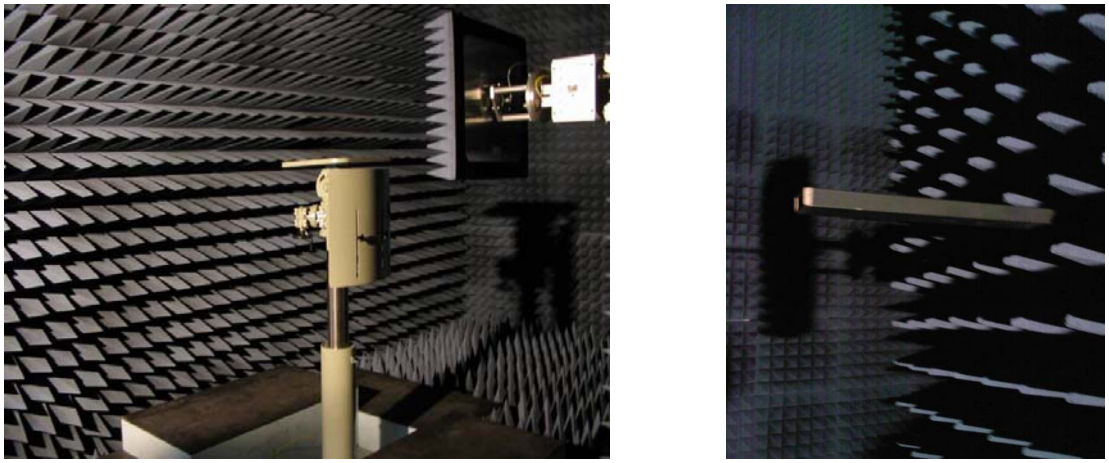

Figure 5.1: The near-field antenna test range of Aselsan Inc.

5.3 E-Plane Radiation Patterns

The radiation pattern measurements are conducted for five different frequencies along the operating band of the slotted waveguide antenna. For being company confidential information for Aselsan Inc., the operating frequency and the bandwidth of the mentioned experimental antenna is prohibited to be disclosed explicitly. Therefore, the equally separated measurement frequencies will be labeled as $0.98f_1, 0.99f_1, f_1, 1.01f_1$ and $1.02f_1$ with f_1 being the center frequency of the antenna at X-band. Recall from the previous chapter that f_1 is also the center frequency of the slot FSS-1 and slot FSS-2 radomes. The center frequency of the single polarized loop FSS, f_2 is slightly larger than f_1 ($f_2 = 1.05f_1$).

The FSS radome prototype to be tested has been integrated to antenna aperture such that the aperture of the antenna is completely covered with the FSS radomes. Some foam spacers have been used between the antenna and the FSS radome in all cases. The antenna-FSS separation is optimized after some measurements at the center frequency.

Normalized E-plane amplitude patterns of the antenna with/without slot FSSs are given in Figures 5.2, 5.3, 5.4, 5.5 and 5.6 for frequencies $0.98f_1$ to $1.02f_1$, respectively.

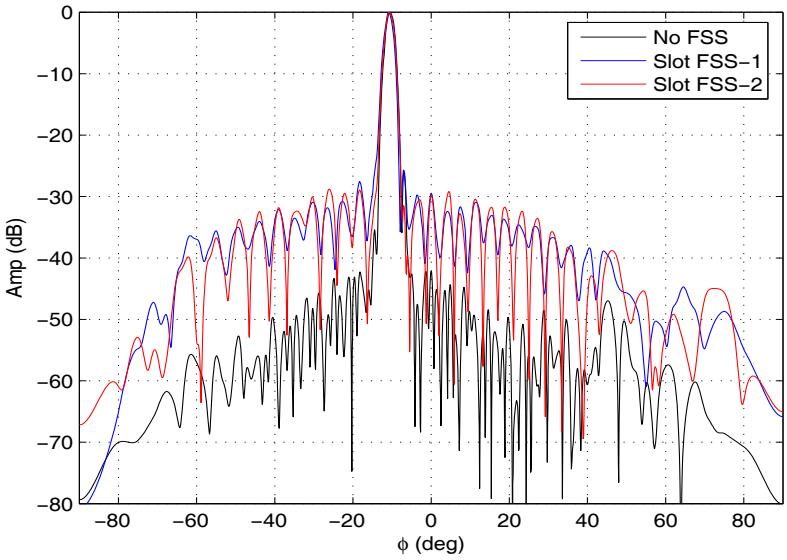

Figure 5.2: Normalized E-plane amplitude patterns with/without slot FSS-1 and slot FSS-2 radomes, $f = 0.98 f_1$

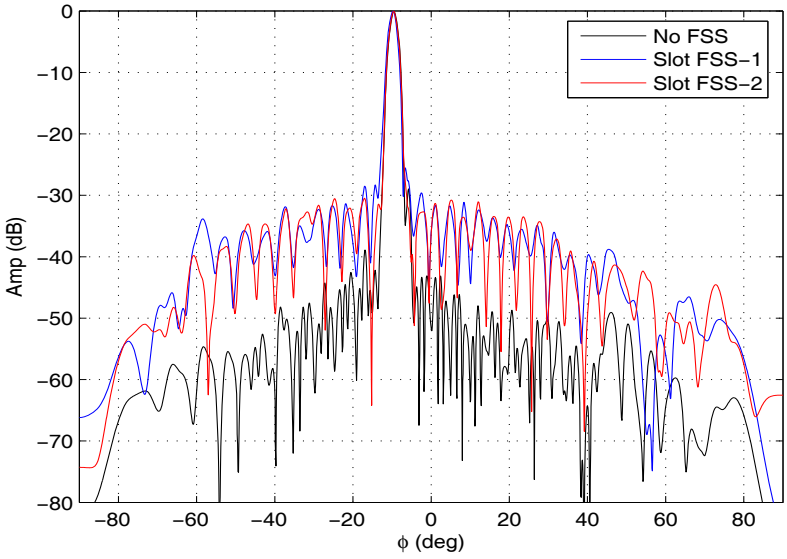

Figure 5.3: Normalized E-plane amplitude patterns with/without slot FSS-1 and slot FSS-2 radomes, $f = 0.99 f_1$

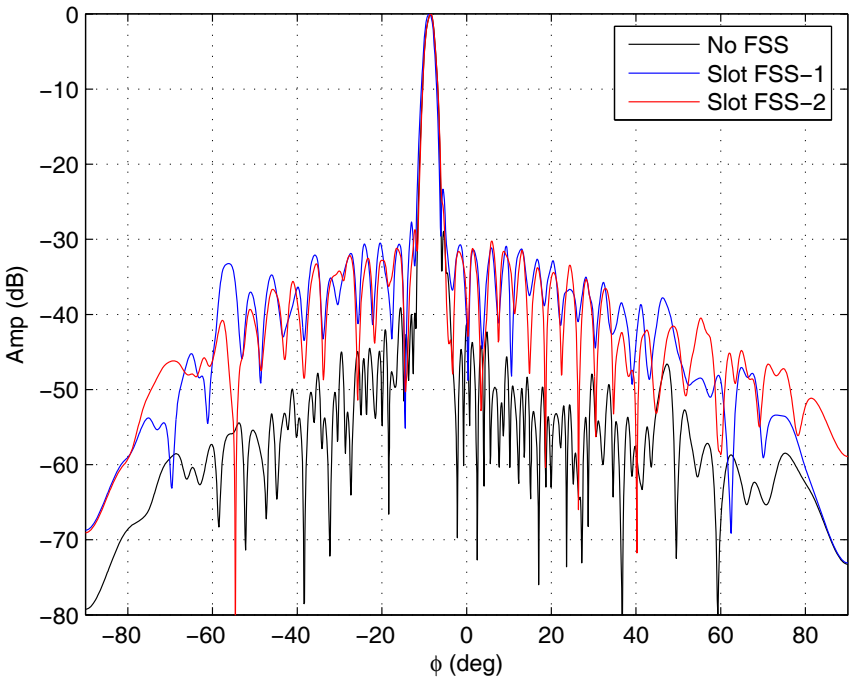

Figure 5.4: Normalized E-plane amplitude patterns with/without slot FSS-1 and slot FSS-2 radomes, $f = f_1$

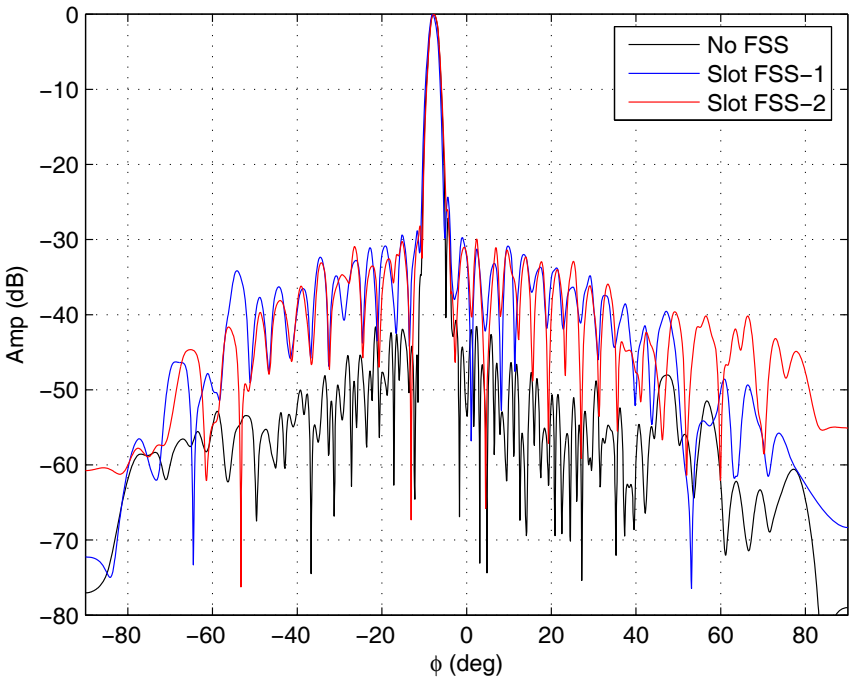

Figure 5.5: Normalized E-plane amplitude patterns with/without slot FSS-1 and slot FSS-2 radomes, $f = 1.01 f_1$

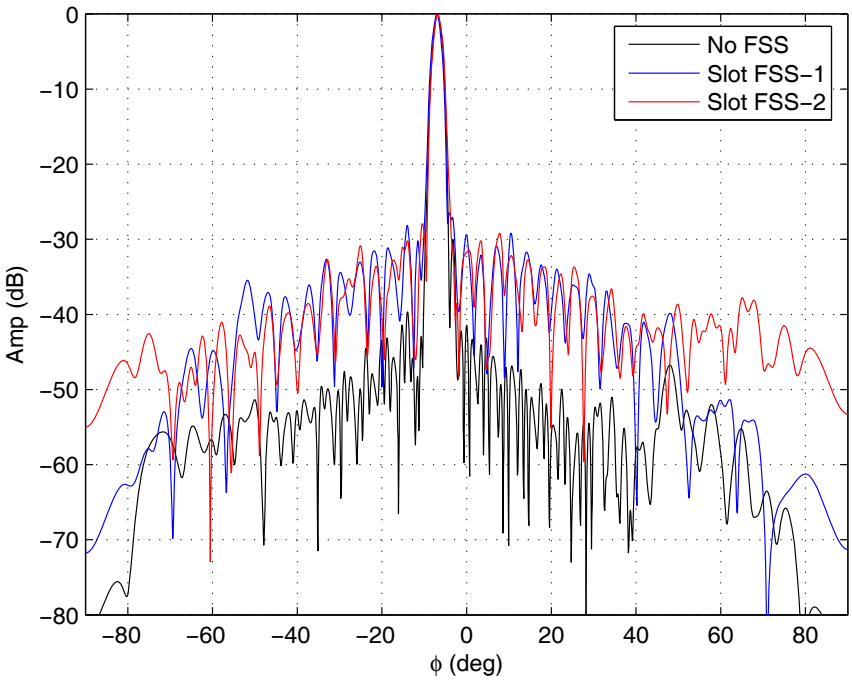

Figure 5.6: Normalized E-plane amplitude patterns with/without slot FSS-1 and slot FSS-2 radomes, $f = 1.02f_1$

The main-beam direction and half-power beamwidth of the antenna is kept constant when slot FSS-1 or slot FSS-2 radome is integrated to the antenna. Peak side-lobe level (SLL), which is about -40dB for the antenna itself, increases to -30dB with the implementation of slot FSS radomes.

The measured antenna patterns with/without single polarized loop FSS radome are plotted in Figures 5.7, 5.8, 5.9, 5.10 and 5.11 for frequencies $0.98f_1$ to $1.02f_1$, respectively.

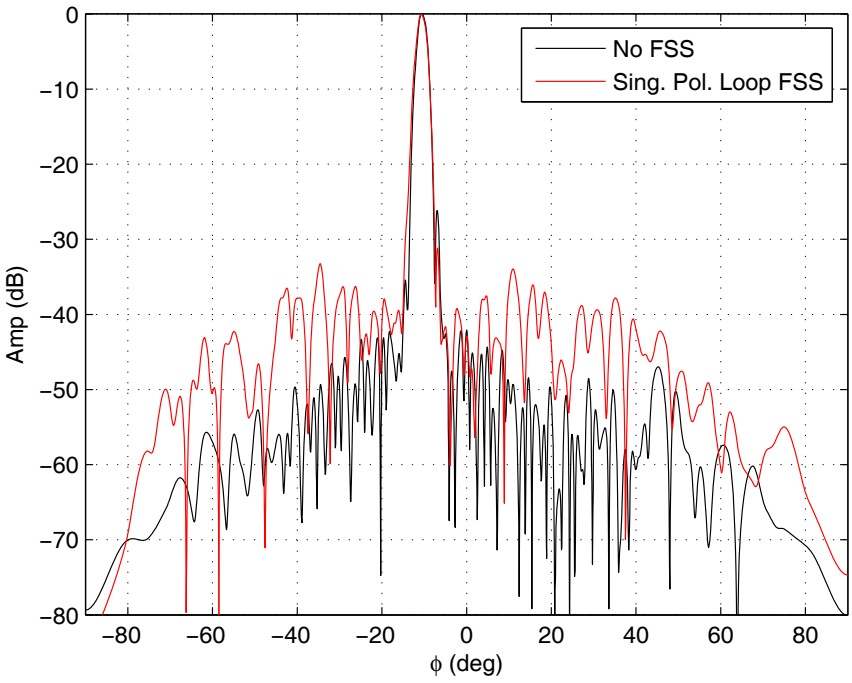

Figure 5.7: Normalized E-plane amplitude patterns with/without single polarized loop FSS radome, $f = 0.98f_1$

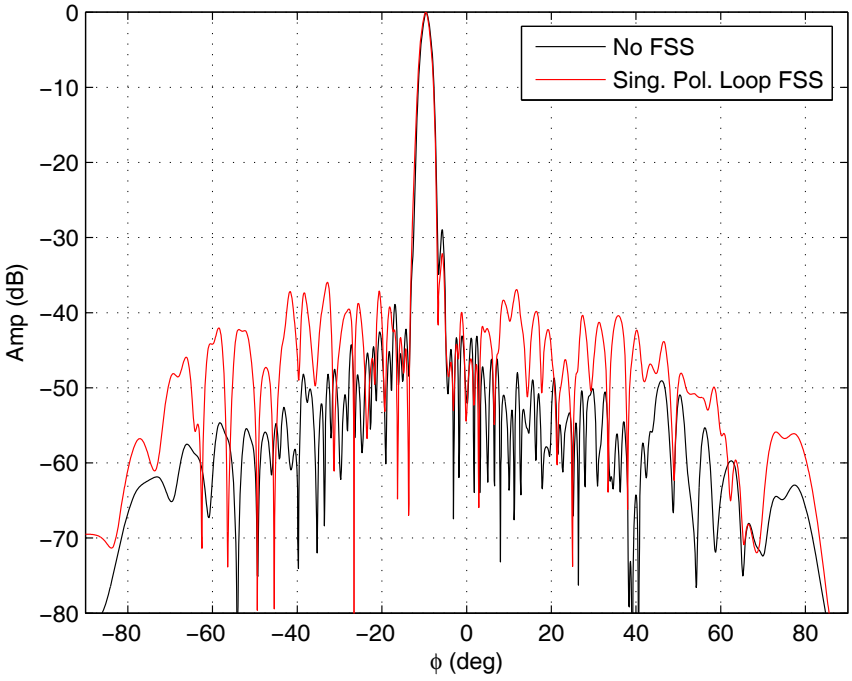

Figure 5.8: Normalized E-plane amplitude patterns with/without single polarized loop FSS radome, $f = 0.99f_1$

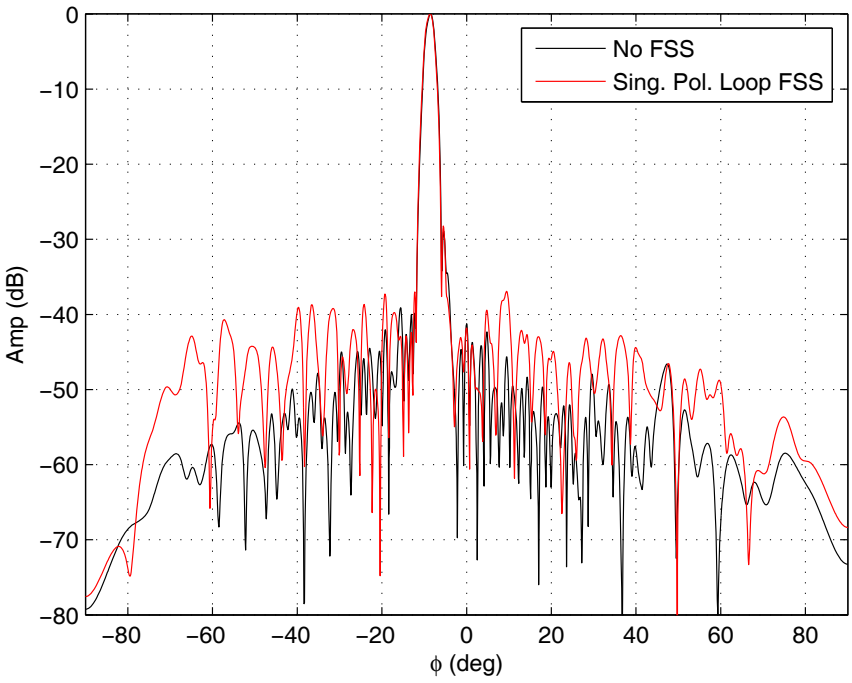

Figure 5.9: Normalized E-plane amplitude patterns with/without single polarized loop FSS radome, $f = f_1$

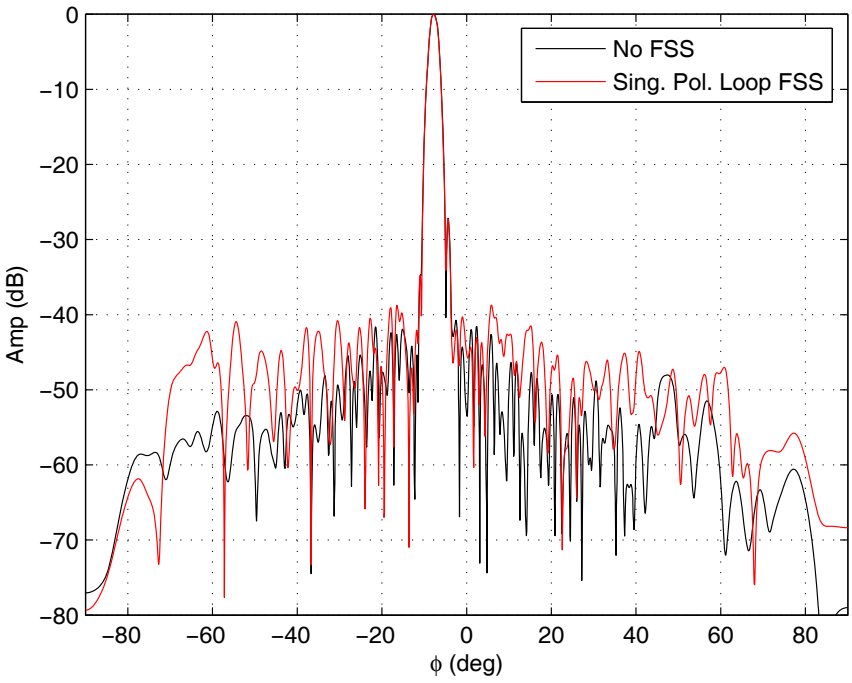

Figure 5.10: Normalized E-plane amplitude patterns with/without single polarized loop FSS radome, $f = 1.01 f_1$

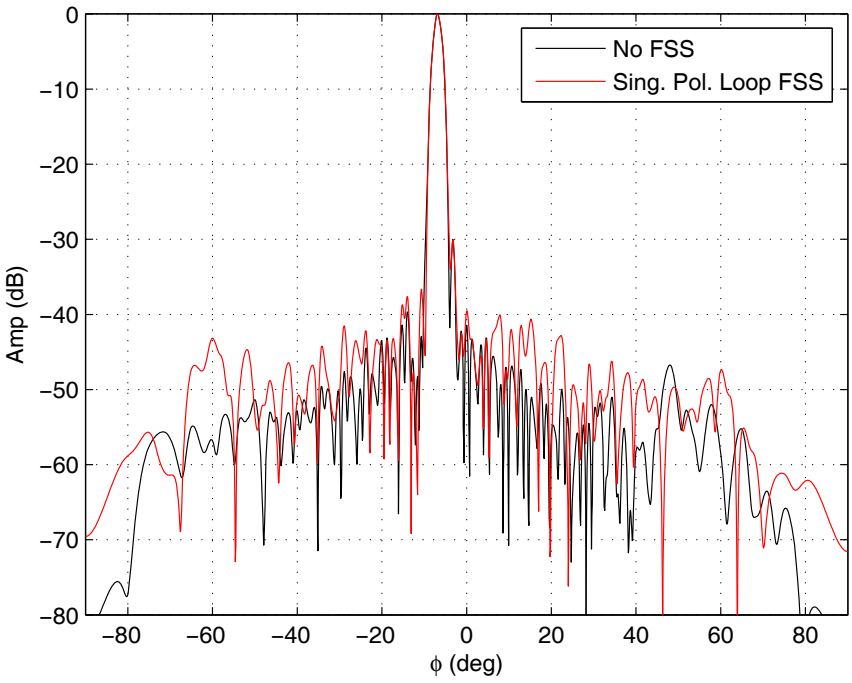

Figure 5.11: Normalized E-plane amplitude patterns with/without single polarized loop FSS radome, $f = 1.02f_1$

Figures 5.7, 5.8, 5.9, 5.10 and 5.11 show that the main-beam direction and half-power beamwidth of the antenna is kept constant with/without single polarized loop FSS. Peak side-lobe level (SLL), which is about -40dB for the antenna itself, increases to -35dB with the implementation of loop FSS radome. No squint is observed in the main beam.

5.4 H-Plane Radiation Patterns

H-plane (elevation) radiation pattern measurements of the antenna with/without FSS radome prototypes have been conducted with the same measurement settings as in E-plane (azimuth) measurements. Actually, one measurement is enough to obtain both E-plane and H-plane patterns in near-field test range in contrast with the far-field measurement techniques. Measured H-plane antenna

patterns with/without slot FSS radomes are given in Figures 5.12, 5.13, 5.14, 5.15 and 5.16 for frequencies $0.98f_1$ to $1.02f_1$.

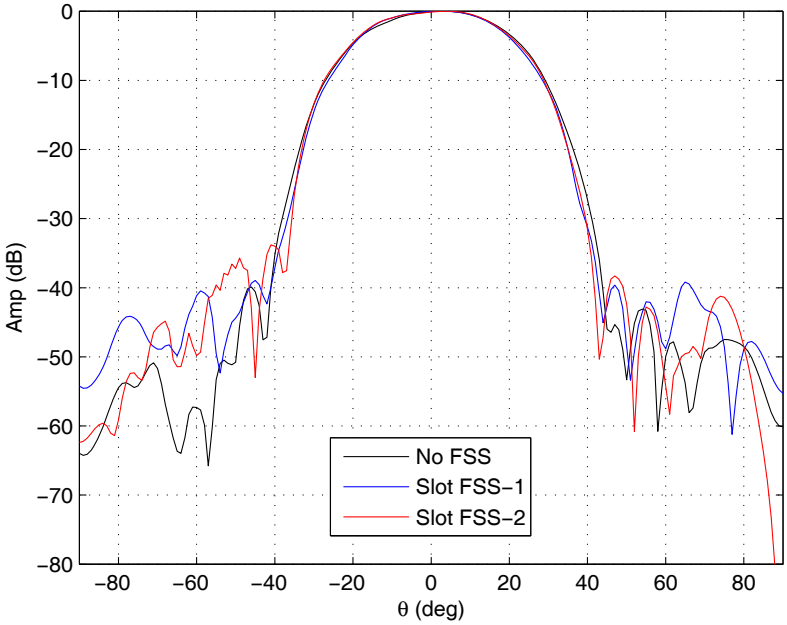

Figure 5.12: Normalized H-plane amplitude patterns with/without slot FSS-1 and slot FSS-2 radomes, $f = 0.98f_1$

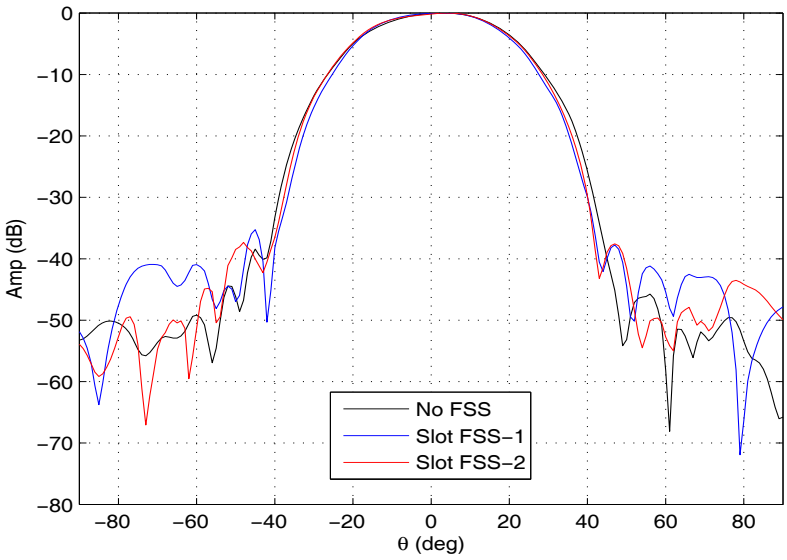

Figure 5.13: Normalized H-plane amplitude patterns with/without slot FSS-1 and slot FSS-2 radomes, $f = 0.99f_1$

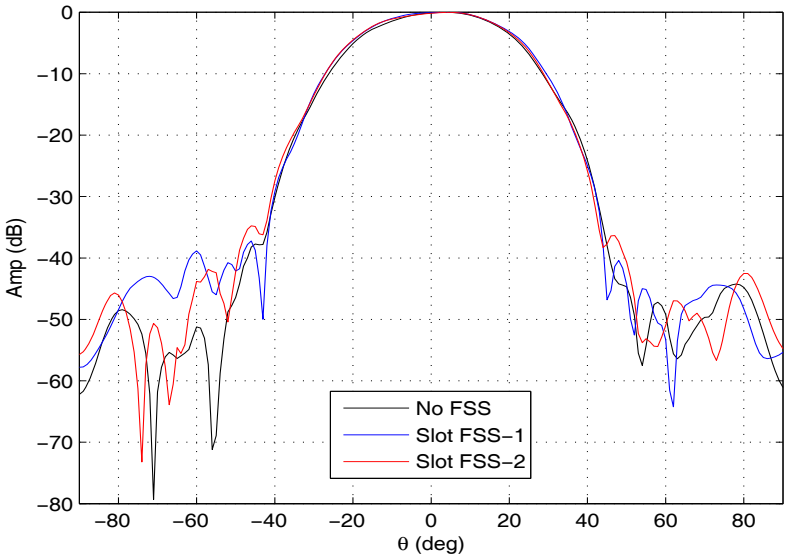

Figure 5.14: Normalized H-plane amplitude patterns with/without slot FSS-1 and slot FSS-2 radomes, $f = f_1$

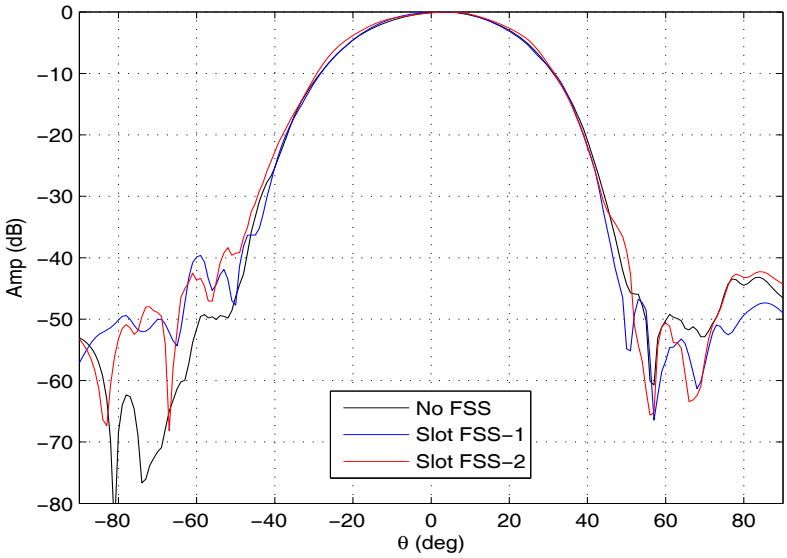

Figure 5.15: Normalized H-plane amplitude patterns with/without slot FSS-1 and slot FSS-2 radomes, $f = 1.01f_1$

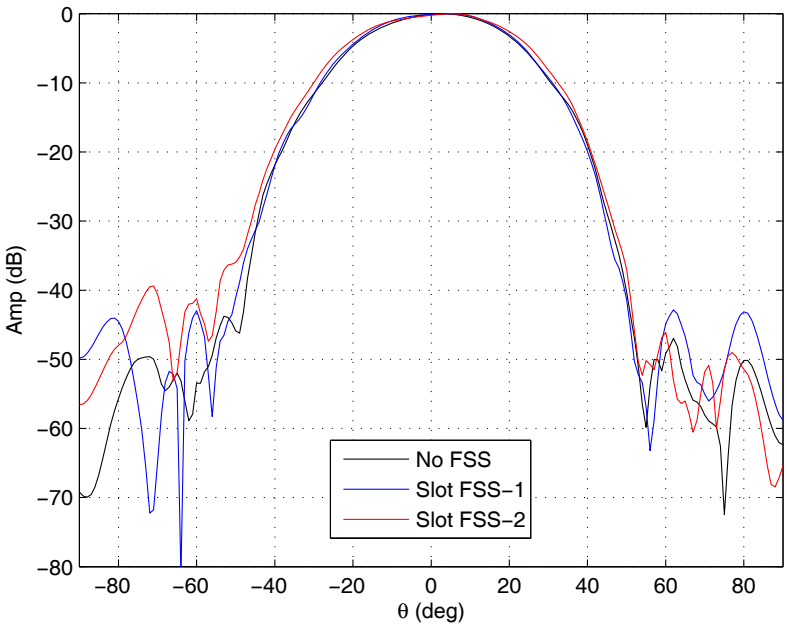

Figure 5.16: Normalized H-plane amplitude patterns with/without slot FSS-1 and slot FSS-2 radomes, $f = 1.02f_1$

The H-plane (elevation) patterns of the antenna with/without slot FSS radomes show excellent agreement as seen above. Half-power beamwidth, side-lobe level and main beam directions do not change with the integration of slot FSS radomes.

Similarly, the integration of single polarized loop FSS radome does not cause any change in the H-plane pattern of the antenna. Measured H-plane patterns are presented in Figures 5.17, 5.18, 5.19, 5.20 and 5.21 for the loop FSS case.

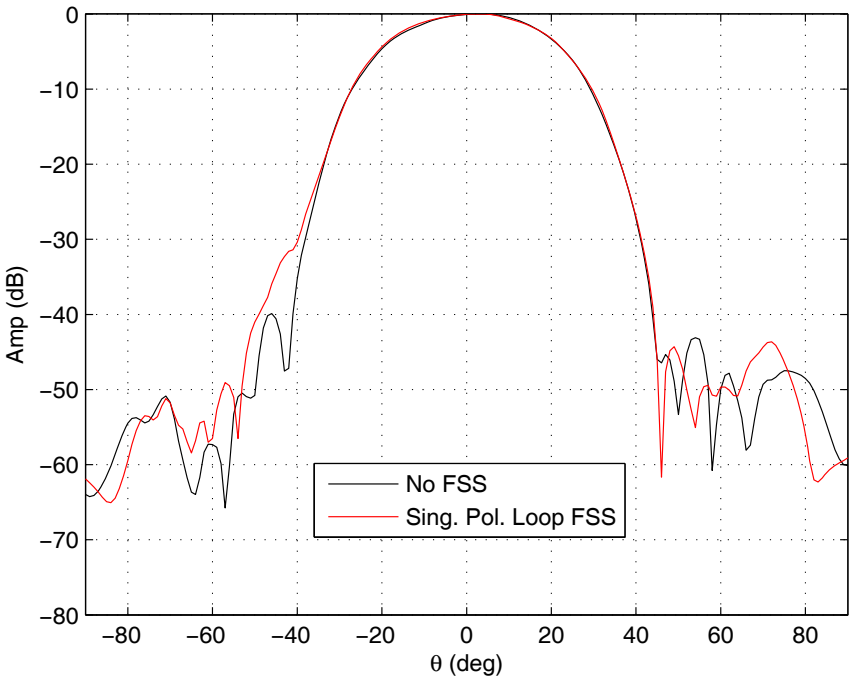

Figure 5.17: Normalized H-plane amplitude patterns with/without single polarized loop FSS radome, $f = 0.98 f_1$

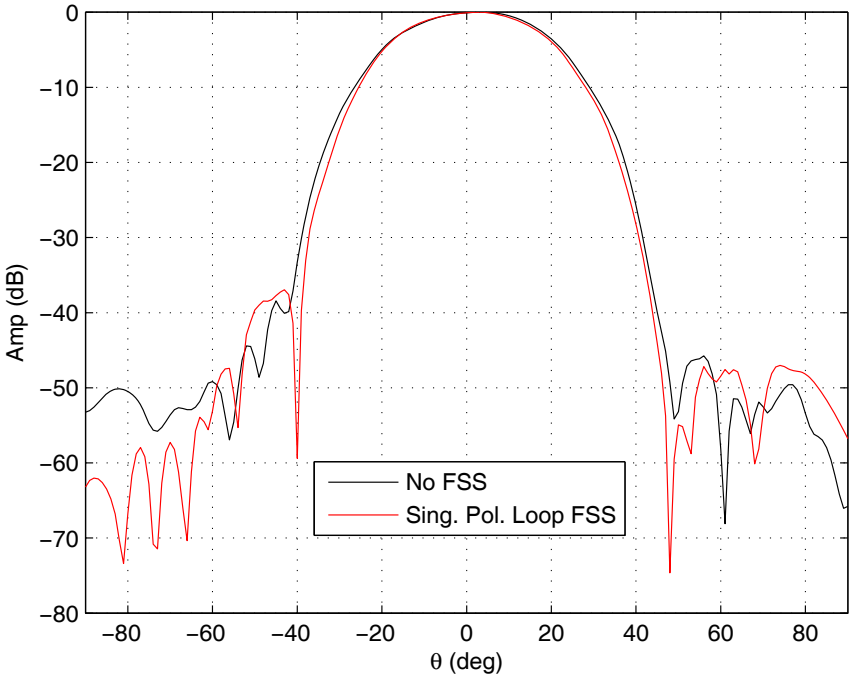

Figure 5.18: Normalized H-plane amplitude patterns with/without single polarized loop FSS radome, $f = 0.99 f_1$

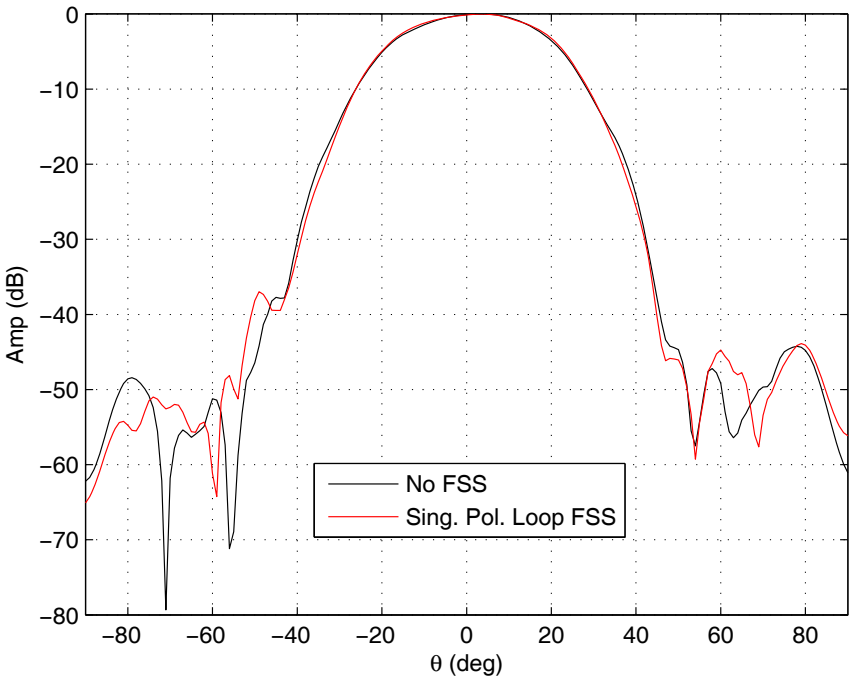

Figure 5.19: Normalized H-plane amplitude patterns with/without single polarized loop FSS radome, $f = f_1$

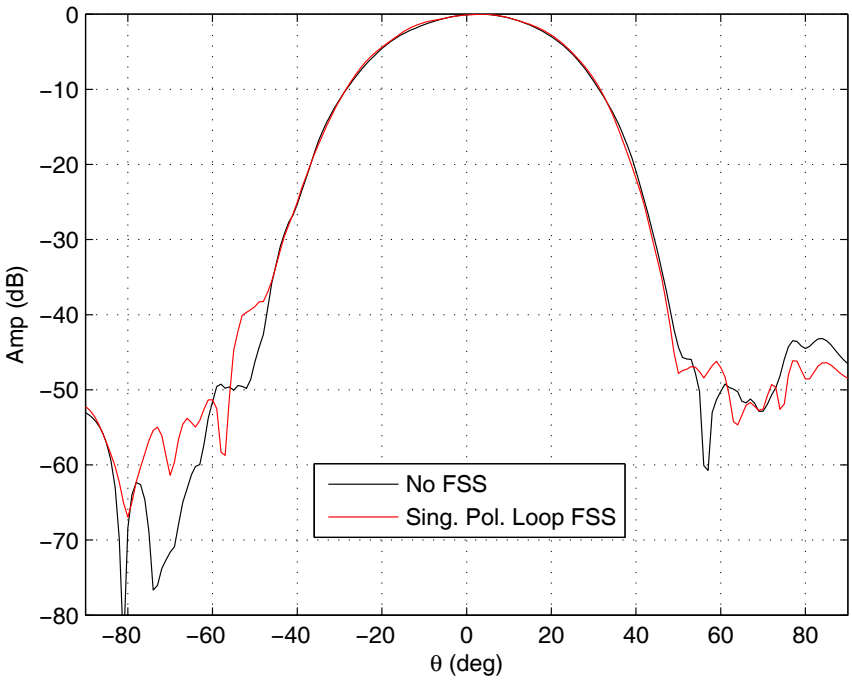

Figure 5.20: Normalized H-plane amplitude patterns with/without single polarized loop FSS radome, $f = 1.01 f_1$

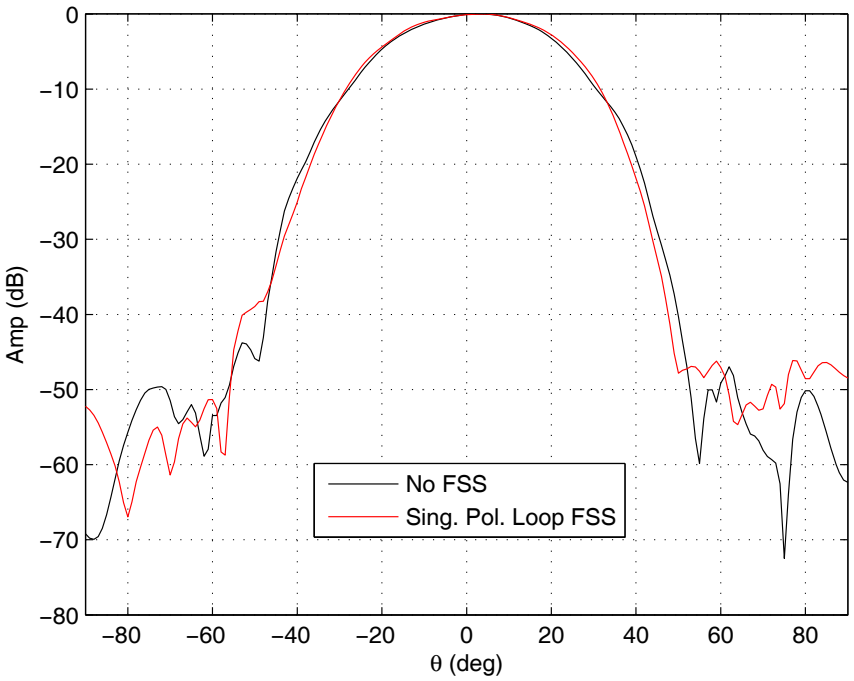

Figure 5.21: Normalized H-plane amplitude patterns with/without single polarized loop FSS radome, $f = 1.02f_1$

5.5 Discussions

An FSS radome is intended to leave the electrical performance of the enclosed antenna unaffected; however, in practice its presence may introduce a perturbation on antenna performance in terms of an increase in the side lobe level, reduction of polarization purity, and tilting of the main beam [34].

In this chapter, three fabricated planar FSS radome prototypes have been investigated in terms of their effects on the radiation performance of a very narrow-beam slotted waveguide array (SWGA) antenna. Results of the E-plane pattern measurements presented in Section 5.3 show that slot FSS-1 and slot FSS-2 radomes have increased the side-lobe level (SLL) of the antenna from -40dB to about -30dB. Direction of maximum radiation and half-power beamwidth do

not change with these slot FSS radomes. It can be clearly concluded that the performance of the single polarized loop FSS radome is much better than that of either of the slot FSSs. Single polarized loop FSS radome increases SLL only about 5dB. Neither the main beam direction nor the half-power beamwidth change for the loop FSS case. Furthermore, the input impedance of the antenna does not change remarkably with the integration of FSS radome prototypes when the separation between the antenna and the FSS radome is optimized.

Table 5.1 shows the cross-polarization levels of the antenna with/without FSS radomes measured at frequencies $0.98f_1$ to $1.02f_1$. The reduction of polarization purity is below 3dB for all cases.

	$0.98f_1$	$0.99f_1$	f_1	$1.01f_1$	$1.02f_1$
No FSS	30.59	32.00	32.29	32.48	33.26
Slot FSS-1	30.06	30.72	29.75	31.37	32.95
Sing. Pol. Loop FSS	27.35	29.84	30.78	31.13	32.19

Table 5.1: Measured cross polarization rejection levels in dB

When H-plane patterns in Section 5.4 are examined, it is evident that neither of the FSS radomes affects the antenna radiation performance in elevation.

The half-power beamwidth of the slotted waveguide antenna is much narrower in E-plane (azimuth) than that in H-plane (elevation). The aperture of the antenna under test is approximately 1 meter long by 10cm high. Antenna elements have an amplitude taper in E-plane to satisfy SLL < -40dB condition. Therefore, small scale perturbations caused by the presence of the FSS structure modify the slot admittances causing a disturbance in the amplitude taper along E-plane through the aperture of the SWGA. This causes an increase in the side lobe levels of the E-plane far-field antenna patterns. It is also observed that reactive effects of the single polarized loop FSS have negligible perturbations on the slot admittances of the antenna array nearby the center frequency of the FSS radome ($0.95f_2 < f < 1.05f_2$). The possibility of the FSS radome to have

fabrication errors in the elevation is less when compared to that in horizontal direction. As a result, antenna patterns with/without FSS radomes agree better in elevation compared to those in azimuth.

Chapter 6

Conclusions

In this thesis, different types of band-pass frequency selective surfaces (FSS) comprising slot elements and modified loop elements, namely single polarized loop FSS, have been extensively studied with their applications to hybrid FSS radomes. These surfaces have been the subject of intensive investigation for their widespread applications as spatial microwave and optical filters.

In Chapter 2, unit element parameters as well as the dielectric profile of the FSS structures have been numerically analyzed by unit cell simulation. A comparative investigation of different FSS types is provided with a detailed parametric study. Effects of cascading periodic arrays and dielectric loading on the transmission curves have been presented with numerical results.

In Chapter 3, several dielectric measurement techniques have been briefly explained. Throughout them, free-space measurement technique is employed for the modeling of dielectric materials to be used in hybrid FSS radome design. It has been observed that RO4003C® - the supporting material of the FSS sheets has a dielectric constant of approximately 3.85 at X-band although it is stated as 3.38 by the manufacturer. Accurate measurement of dielectric properties of a

material and proper characterization of them in the analysis play a crucial role in an FSS radome design.

Making use of the dielectric measurement results, three different hybrid FSS radomes have been designed, fabricated, tested and compared in Chapter 4. Two of these radomes are based on slot elements with different inter-element spacings, namely slot FSS-1 and slot FSS-2; the third is a modified loop FSS (named single polarized loop FSS) radome unique to this work. A conventional polarization independent square loop FSS has been modified in such a way that one of the polarizations is eliminated by placing thin conductors on the corresponding gaps (i.e. top and bottom gaps to remove vertical polarization) of the loop. Good agreement has been achieved between numerical and experimental results for all FSSs. It has been observed that slot FSSs of nearly same slot length and different inter-element spacing yield resonances around the same center frequency with different bandwidths. The single polarized loop FSS has much broader bandwidth than the two slot FSSs. This difference is believed to be the result of enhanced electric coupling between the adjacent conductors of loop FSS. However, the out-of-band rejection of single polarized loop FSS is not as much as that of the slot FSSs. The differences of slot based and loop based FSSs in terms of their operational bandwidth and out-of-band rejection levels can make them preferable for different applications.

In Chapter 5, radiation pattern measurements of the slotted waveguide array antenna (SWGA) have been performed with/without FSS radome prototypes in addition to transmission response measurements of Chapter 4. In contrast with most of the published work which offer only free-space transmission/reflection curves; we present radiation performance measurements with the FSS radomes as well. The H-plane (elevation) measurement results show that antenna elevation patterns with/without FSS radome excellently match each other. However, it is observed that the E-plane (azimuth) patterns have been destroyed to some extent

with the integration of slot FSS-1 and slot FSS-2 radomes to the SWGA. Single polarized loop FSS radome has performed pretty good for E-plane in addition to H-plane. Main lobe of the antenna has remained unchanged with the single polarized loop FSS. Maximum side-lobe level increase in the azimuth is below 5dB for all frequencies.

Adaptation of hybrid FSS radome to the slotted waveguide antenna has been achieved without any significant reduction in the radiation performance. The antenna with hybrid FSS radome, which is transparent at antenna operating frequencies and opaque at other frequencies, has the advantage of superior mechanical durability as well as reduced out-of-band radar cross section (RCS). As a future work, this study can be extended to the designs of conformal FSS structures for curved platforms. Also, by cascading FSS layers of different resonant frequencies, designs with multiple transmission bands can be achieved. Moreover, by employing PIN diode switches, frequency responses and polarization properties of these structures can be electronically controlled.

Appendix A

Floquet's Theorem

Let us consider a wave propagating in periodic structures, which may be characterized by periodic boundary conditions or a periodically varied dielectric constant. We note that the fields at a point z in an infinite periodic structure differ from the fields one period L away by a complex constant. This is obviously true because in an infinite periodic structure, there should be no difference between the fields at z and at $z + L$ except for the constant attenuation and phase shift. Let a function $u(z)$ represent a wave. Then a wave $u(z)$ at z and a wave $u(z + L)$ at $z + L$ are related in the same manner as a wave $u(z + L)$ at $z + L$ and a wave $u(z + 2L)$ at $z + 2L$.

Mathematically, we write

$$\frac{u(z+L)}{u(z)} = \frac{u(z+2L)}{u(z+L)} = \frac{u(z+mL)}{u(z+(m-1)L)} = C. \tag{A.1}$$

From this we obtain

$$u(z+mL) = C^m u(z). \tag{A.2}$$

The constant C is in general complex, which we write

$$C = e^{-j\beta L}, \qquad \beta = \text{complex}, \tag{A.3}$$

and β represents the propagation constant.

Now let us consider a function

$$R(z) = e^{j\beta z}u(z). \tag{A.4}$$

Then $R(z+L) = e^{j\beta(z+L)}u(z+L) = R(z)$. Therefore, $R(z)$ is a periodic function of z with the period L, and thus can be represented in a Fourier series.

$$R(z) = \sum_{n=-\infty}^{\infty} A_n e^{-j(2n\pi/L)z}. \tag{A.5}$$

Using (A.4), we finally obtain a general expression for a wave in a periodic structure with the period L.

$$\begin{aligned} u(z) &= \sum_{n=-\infty}^{\infty} A_n e^{-j(\beta+2n\pi/L)z} \\ &= \sum_{n=-\infty}^{\infty} A_n e^{-j\beta_n z}, \quad \beta_n = \beta + \frac{2n\pi}{L}. \end{aligned} \tag{A.6}$$

Noting that, in general, the wave consists of both positive-going and negative-going waves, we write

$$u(z) = \sum_{n=-\infty}^{\infty} A_n e^{-j\beta_n z} + \sum_{n=-\infty}^{\infty} B_n e^{+j\beta_n z}. \tag{A.7}$$

This is a representation of a wave in periodic structures in a form of an infinite series, resembling harmonic representation ($e^{-j\omega_n t}$) in time. The nth term in (A.6) is called the nth *space harmonic* or *Hartree harmonic* [35]. Equation (A.7) is the mathematical representation of Floquet's theorem, which states that the wave in periodic structures consists of an infinite number of *space harmonics*.

Bibliography

[1] F. O'Nians and J. Matson, "Antenna Feed System Utilizing Polarization Independent Frequency Selective Intermediate Reflector," U.S. Patent 3,231,892, Jan. 25, 1966.

[2] R. Ott, R. Kouyoumjian and L. Peters Jr., "Scattering by a two dimensional periodic array of narrow plates," *Radio Sci.*, vol. 2, pp. 1347-1359, Nov. 1967.

[3] C.C. Chen, "Scattering by a two-dimensional periodic array of conducting plates," *IEEE Trans. Antennas. Propag.*, vol. AP-18, pp. 660-665, Sep. 1970.

[4] C.C. Chen, "Transmission through a conducting screen perforated periodically with apertures," *IEEE Trans. Microwave Theory Tech.*, vol. MTT-18, pp. 627-632, Sep. 1970.

[5] B.A. Munk, R. Kouyoumjian, and L. Peters Jr., "Reflection Properties of Periodic Surfaces of Loaded Dipoles," *IEEE Trans. Antennas. Propag.*, vol. AP-19, pp. 612-617, Sep. 1971.

[6] B.A. Munk, and R.J. Luebbers, "Reflection Properties of Two-Layer Dipole Arrays," *IEEE Trans. Antennas. Propag.*, vol. AP-22, pp. 766-773, Nov. 1974.

[7] G.G. Macfarlane, "Quasi-stationary field theory and its application to diaphragms and junctions in transmission lines and waveguides," *J. Instn. Elect. Engrs.*, vol. 93, Pt. III-A pp. 703-719, 1946.

[8] H.G. Booker, "Slot aerials and their relation to complementary wire aerials (Babinet's principle)," *J. Instn. Elect. Engrs.*, vol. 93, Pt. III-A pp. 620-626, 1946.

[9] B.A. Munk, *Frequency Selective Surfaces: Theory and Design.* John & Wiley Sons, Canada, 2000.

[10] J. Huang, T. Wu, and S. Lee, "Tri-band frequency selective surface with circular ring elements," *IEEE Trans. Antennas. Propag.*, vol. 42, pp. 166-175, Feb. 1994.

[11] R. Mittra, C.H. Chan, and T. Cwik, "Techniques for analyzing frequency selective surfaces-a review," *Proc. IEEE*, vol. 76, pp. 1593-1615, Dec. 1988.

[12] J. Romeu and Y. Rahmat-Samii, "Fractal FSS: A novel dual-band frequency selective surface," *IEEE Trans. Antennas Propag.*, vol. 48, pp. 1097-1105, Jul. 2000.

[13] B. Schoenlinner, A. Abbaspour-Tamijani, L.C. Kempel, and G.M. Rebeiz, "Switchable low-loss RF MEMS Ka-band frequency-selective surface," *IEEE Trans. Microw. Theory Tech.*, vol. 52, pp. 2474-2481, Nov. 2004.

[14] E.A. Parker and S.B. Savia, "Active frequency selective surfaces with ferroelectric substrates," *Proc. Inst. Elect. Eng. Microwaves, Antennas and Propagation*, vol. 148, pp. 103-108, Apr. 2001.

[15] D. Zhang, Y. Rahmat-Samii, H.R. Fetterman, S. Prakash, R.F. Bunshah, M. Eddy, and J.L. Nilsson, "Application of high Tc superconductors and frequency selective surfaces: Experiment and theory," *IEEE Trans. Microw. Theory Tech.*, vol. 41, pp. 1032-1036, Jun./Jul. 1993.

[16] D.C. Jenn, *Radar and Laser Cross Section Engineering.* American Institute of Aeronautics and Astronautics, Virginia, 2005.

[17] Y.E. Erdemli, K. Sertel, R.A. Gilbert, D.E. Wright, and J.L. Volakis, "Frequency selective surfaces to enhance performance of broad band reconfigurable arrays," *IEEE Trans. Antennas Propag.*, vol. 50, pp. 1716-1724, Dec. 2002.

[18] H.J. Visser and M. Guglielmi, "Filter design of waveguide array antennas," *IEEE AP-S Symp. Digest*, vol. 4, pp. 2338-2341, Jul. 1997.

[19] S. Monni, N.L. Juan, A. Neto, and G. Gerini, "Phased array antenna integrated with a frequency selective surface - theory and experiments," *Phased Array Systems and Technology, IEEE AP-S Symp. Digest*, pp. 458-463, Oct. 2003.

[20] G. Gerini and L. Zappelli, "Multilayer array antennas with integrated frequency selective surfaces conformal to a circular cylindrical surface," *IEEE Trans. Antennas Propag.*, vol. 53, no. 6, pp. 2020-2030, Jun. 2005.

[21] M.G. Floquet, "Sur les equations différentielles linéaires a coefficients périodiques," *Annale École Normale Superiur*, pp. 47-88, 1883.

[22] R.J. Luebbers and B.A. Munk, "Some Effects of Dielectric Loading on Periodic Slot Arrays," *IEEE Trans. Antennas Propag.*, vol. AP-26, no. 4, pp. 536-542, Jul. 1978.

[23] C.A. Balanis, *Advanced Engineering Electromagnetics*. John & Wiley Sons, Canada, 1989.

[24] D.M. Pozar, *Microwave Engineering*. John & Wiley Sons, New York, 1998.

[25] Application Note on Basics of Measuring the Dielectric Properties of Materials - http://cp.literature.agilent.com/litweb/pdf/5989-2589EN.pdf, Agilent Technologies, USA, June 2006.

[26] Free-Space Materials Measurement Seminar - http://www.home.agilent.com/upload/cmc-upload/All/FreeSpaceSeminarRev2.pdf, Agilent Technologies, USA, June 2005.

[27] D.V. Blackham and R.D. Pollard, "An Improved Technique for Permittivity Measurements Using a Coaxial Probe," *IEEE Trans. Instr. Meas.*, vol. 46, pp. 1093–1099, Oct. 1997.

[28] D.K. Ghodgaonkar, V.V. Varadan and V.K. Varadan, "Free-Space Measurement of Complex Permittivity and Complex Permeability of Magnetic Materials at Microwave Frequencies," *IEEE Trans. Instr. Meas.*, vol. 39, pp. 387–394, Apr. 1990.

[29] D.K. Ghodgaonkar, V.V. Varadan and V.K. Varadan, "A Free-Space Method for Measurement of Dielectric Constants and Loss Tangents at Microwave Frequencies," *IEEE Trans. Instr. Meas.*, vol. 37, pp. 789–793, Jun. 1989.

[30] N. Gagnon, *Design and Study of a Free-Space Quasi-Optical Measurement System,* MSc Thesis, University of Ottowa Dept. of Electrical and Computer Engineering, Canada, May 2002.

[31] N. Gagnon, J. Shaker, P. Berini, L. Roy and A. Petosa, "Material Characterization Using a Quasi-Optical Measurement System," *IEEE Trans. Instr. Meas.*, vol. 52, pp. 333–336, Apr. 2003.

[32] Y.N. Noskov, "Method for Measuring Properties of High Relative Dielectric Constant Materials in a Cutoff Waveguide Cavity," *IEEE Trans. Microwave Theory Tech.*, vol. 48, pp. 329–333, Mar. 2000.

[33] Agilent 85071E Materials Measurement Software - http://cp.literature.agilent.com/litweb/pdf/5988-9472EN.pdf, Agilent Technologies, USA, June 2006.

[34] E. Martini, F. Caminita, M. Nannetti and S. Maci "Fast analysis of FSS radome for antenna RCS reduction ," *IEEE AP-S Symp. Digest*, vol. 9-14, pp. 1801–1804, Jul. 2006.

[35] A. Ishimaru, *Electromagnetic Wave Propagation, Radiation and Scattering.* Prentice Hall, New Jersey, 1991.

[36] CST Microwave Studio® 2008, https://www.cst.com/Contents/Products/MWS/Overview.aspx, CST - Computer Simulation Technology AG, Darmstadt, Germany.

[37] RO4003C® High Frequency Laminate Datasheet - http://www.rogerscorporation.com/mwu/pdf/RO4000data_fab_10_07.pdf, Rogers Corporation, Chandler, AZ.

[38] ROHACELL® Performance Polymer Datasheet - http://www.rohacell.com/en/performanceplastics8344.html, Evonik Industries, Chandler, AZ.